



UNIVERSITÀ DI PISA

Department of Physics  
Masters Degree in Physics

# Characterization of monolithic CMOS pixel sensors for charged particle detectors and for high intensity dosimetry

**6 Candidate:**  
Ravera Eleonora

Supervisor:  
Francesco Forti

7 Academic year 2021/2022

# <sup>8</sup> Contents

<sup>9</sup> <b>1 Arcadia-MD1</b>	<b>3</b>
10    1.1 The sensor and the front end . . . . .	4
11    1.2 Readout logic and data structure . . . . .	5
12      1.2.1 Matrix division and data-packets . . . . .	5
13      1.2.2 Matrix division and data-packets . . . . .	6
<sup>14</sup> <b>2 Characterization</b>	<b>9</b>
15    2.1 TJ-Monopix1 characterization . . . . .	9
16      2.1.1 Threshold and noise: figure of merit for pixel detectors . . . . .	9
17      2.1.2 Linearity of the ToT . . . . .	13
18      2.1.3 Calibration of the ToT . . . . .	14
19      2.1.4 Changing the bias . . . . .	19
20      2.1.5 Measurements with radioactive sources . . . . .	20
21      2.1.6 Dead time measurements . . . . .	25
22    2.2 ARCADIA-MD1 characterization . . . . .	27
<sup>23</sup> <b>3 Test beam measurements</b>	<b>31</b>
24    3.1 Apparatus description . . . . .	32
25      3.1.1 Accelerator . . . . .	32
26      3.1.2 Mechanical carriers . . . . .	32
27    3.2 Measurements . . . . .	33
<sup>28</sup> <b>Bibliography</b>	<b>38</b>

<sup>29</sup> **Chapter 1**

<sup>30</sup> **Arcadia-MD1**

<sup>31</sup> [16] [17]

<sup>32</sup> ARCADIA (Advanced Readout CMOS Architectures with Depleted Integrated sensor  
<sup>33</sup> Arrays) and SEED (Sensor with Embedded Electronic Developement) are both groups  
<sup>34</sup> involved in the development of MAPS sensors based on the CMOS technology and both  
<sup>35</sup> having LFoundry as industrial partner. Many concept and performances studies have been  
<sup>36</sup> carried out with simulations and small-scale test structure by SEED, before ARCADIA,  
<sup>37</sup> applying the experience developed with SEED to a full chip prototype, the MD1. MA-  
<sup>38</sup> TISSE is an example of small-scale prototypes produced for testing: it is made by  $24 \times 24$   
<sup>39</sup> pixels organised in 4 columns; each pixel has an analog output, which allows for energy  
<sup>40</sup> loss measurements, and a shutter snapshot readout with a speed that can reach 5 MHz.

<sup>41</sup> The ARCADIA target are the development of a novel CMOS sensor platform allowing  
<sup>42</sup> for fully depleted active sensors with thickness in range  $50 \mu\text{m}$  to  $500 \mu\text{m}$ . A small charge  
<sup>43</sup> collecting electrode to achieve a good signal to noise ratio, a high time resolution (the  
<sup>44</sup> lower bound is set at  $O(\mu\text{m})$  but more advanced solutions are investigating for a  $O(10 \text{ ns})$ )  
<sup>45</sup> and a scalable readout architecture with low power consumption are the main requirement  
<sup>46</sup> imposed by ARCADIA; the Main Demonstrator 1, has been submitted in 2020, and its  
<sup>47</sup> characteristic are shown in table 1.1. A second main demonstrator (ARCADIA-MD2) has  
<sup>48</sup> been submitted in Summer 2021, featuring a similar design of MD1 and which is expected  
<sup>49</sup> to be faster and to have a lower power consumption thanks to a logic and buffering  
<sup>50</sup> optimisation.

Parameter	Value
Matrix size	$\times \text{ cm}^2$
Pixel size	$25 \times 25 \mu\text{m}^2$
Depth	$48/100/200 \mu\text{m}$
Electrode size	$9 \times 9 \mu\text{m}^2$
Power consumption	$\sim 10 \text{ mW/cm}^2$

Table 1.1

## 51 1.1 The sensor and the front end

52 ARCADIA-MD1 is an LFoundry chip which implements the CMOS technology in 110 nm  
 53 ???. The standard p-type substrate is replaced by a n-type ??.

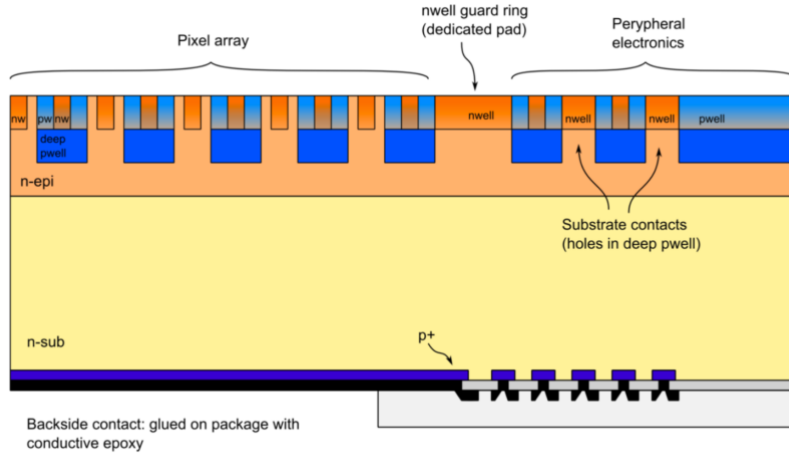


Figure 1.1

53  
 54 The sensor is made by a *p* substrate and an *n* doped diode within a *n* epitaxial layer.  
 55 Being part of DMAPS category, it is operated in fully depletion and the charge is then  
 56 fastly collected by drift. Up to now the sensor has been implemented in three different  
 57 variant: 48  $\mu\text{m}$ , 100  $\mu\text{m}$  and 200  $\mu\text{m}$  thick, each with the same FE and readout logic but  
 58 requiring a diffent biasing.

59 MD1 chips have been submitted in two different front end options: they are commonly  
 60 called ALIPDE-like and bulk-driven. The differences between them are in the FE circuit  
 61 and in the biasing current of the registers, while the underlying readout is the same.  
 62 The main difference is in the amplification stage, while in the ALPIDE-like flavor the  
 63 amplification is implemented as explained in section ??, in the bulk-driven flavor the gain  
 64 is adjusted by the ratio of two transcondutances. Consequently, some of the biasing  
 65 registers, whose current is settable externally by the DAQ, have different default values  
 66 and they might not be available at all in one of the flavor. An example is the ICLIP  
 67 register, which is available only in the bulk driven flavor despite the transistor to which  
 68 refers is implemented in both the flavor; its function is similar to the *curfeed* capacitor in  
 69 figure ??(a), which controls the current in the input branch of the FE and also influences  
 70 the value of tha baseline at the discriminator input.

71 There are three types of configuration registers which are used to configure the matrix:

- 72 • the Pixel Configuration Register, which is a 2-bits word used for enabling respectively the masking and injection functionalities. The on pixel Pixel Configuration Register circuit and how the mask/injection can be enable/disable is shown in figure 1.2.
- 76 • the Internal Configuration Register, which are used for the communication with the 77 FPGA, for example to send a pulse, reset or configure the whole matrix.
- 78 • the Global Configuration Registers, which are used to set the configuration of the 79 FE parameters are similar to the one of the TJ-Monopix1 circuit.

80 Their bias with the one of the sensors are supplied by padframes (a top, a bottom and a  
 81 side one) placed aside the matrix, which also provide the clock, the reset, the test pulse  
 for the injection circuit and the communication signals.

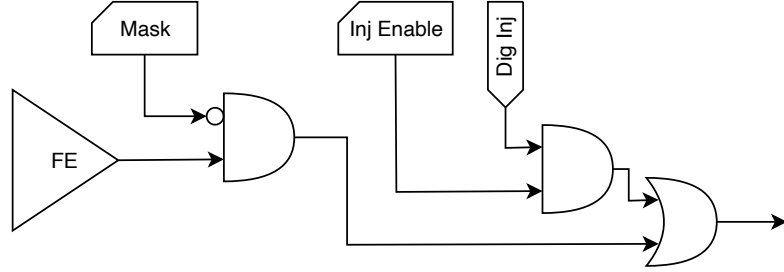


Figure 1.2

82

## 83 1.2 Readout logic and data structure

### 84 1.2.1 Matrix division and data-packets



Figure 1.3: (a) Board hosting the MD1 and (b) FPGA

85 One of the main ambition of the MD1 is to achieve the lowest possible power consump-  
 86 tion, hopefully less than  $20 \text{ mW/cm}^2$ ; this is principally due to the hope of application also  
 87 in space experiment field, where the power consumption and the cooling are for sure an  
 88 issue. In order to undergo that requirement, the matrix is clockless and the readout is  
 89 triggerless; moreover the chip can be operated both in the high rate mode and low rate  
 90 depending on if only one or all serializers, which are placed at the periphery of the matrix  
 91 are enabled or only one is shared between the sections; in addition, to save as much area  
 92 as possible, no buffer have been included on the matrix at the expense of the maximum

Bits	Meaning
31:24	timestamp
23:20	section index
19:16	column index
15:9	pixel region
8:0	bitmap

Table 1.2: Data packet structure implemented by the MD1 readout logic.

hit rate sustainable. The readout then is completely data push and when a hit is received immediately starts the readout mechanism to transmit it off chip.

The board hosting the chip is connected with a breakout board, which is connected to the FPGA; a data packet sent to the EoS, is then encoded and transmitted to the FPGA using a 320 MHz DDR serializers and then transmitted by ethernet to the PC. A photo of the experimental setup is shown in figure ??.

### 1.2.2 Matrix division and data-packets

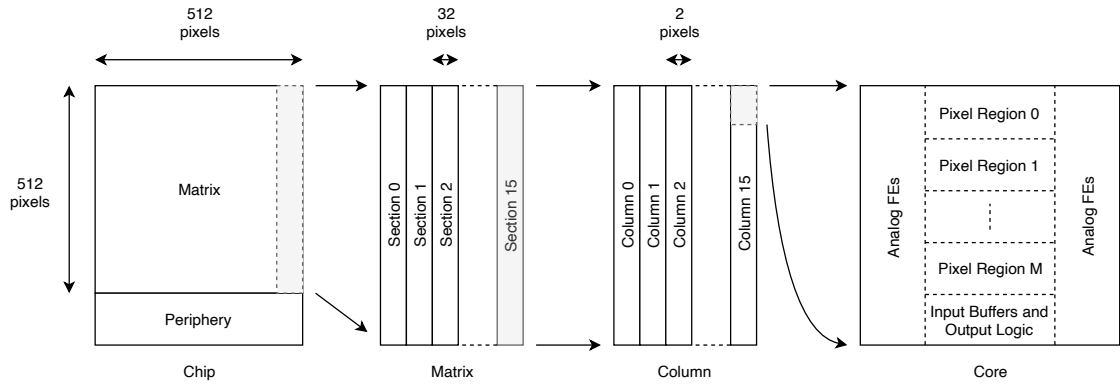


Figure 1.4

Also the chip structure is meant to optimize the power consumption and the scalability for future up-scaling; in particular it is divided into a physical and logical hierarchy, which also reflects in the way the data packets are built (tab.1.2). First of all, the 512 columns are split in 16 sections each one containing  $512 \times 32$  pixels and having its own biasing lines and serializers at the matrix periphery. Each section is divided  $512 \times 2$  double-column mirrored, which just as in TJ-Monopix1, share the same readout buses placed between them and having analog logic on the sides. The rows, then, are divided in groups of 32, resulting in core with  $32 \times 2$  pixels. Finally each core is sub-divided in regions, each one containing  $4 \times 2$  pixels.

The readout has been designed with the constraints of being capable of handling with a hit rate of  $100 \text{ MHz}/\text{cm}^2$ , then it has been optimized to minimize the amount of logic and to have a high bandwidth of transmission of the data to the periphery. For this reason not all pixels have been provided by the readout logic. In particular, each pixel region can either be Master or Slave, depending on if it has or has not the readout capability. The Master's data packets are therefore composed of two parts: the bitmap of the Master itself and the one of Slave. Moreover, the pioneer idea of ARCADIA-MD1, which has as

116 finally goal the test of a readout cabable of transmit cluster data in as few data packets  
 117 as possible, is the possibility of the Master to decide what Slave (top or bottom) read; the  
 118 information of what Slave has been selected is represented by a bit, often called *hot bit*, in  
 119 the data-packet. Every pixel has an associated status register, that essentialaly is a flip flop  
 120 (FF), which is set to 1 when the pixel stores a hit; an OR of the FF whithin the Master  
 121 or the Slave region generates an active flag which is used to require a readout by the EoS.  
 In figure 1.5 is shown the circuit with the logic of assignment of the Slave to the Master.

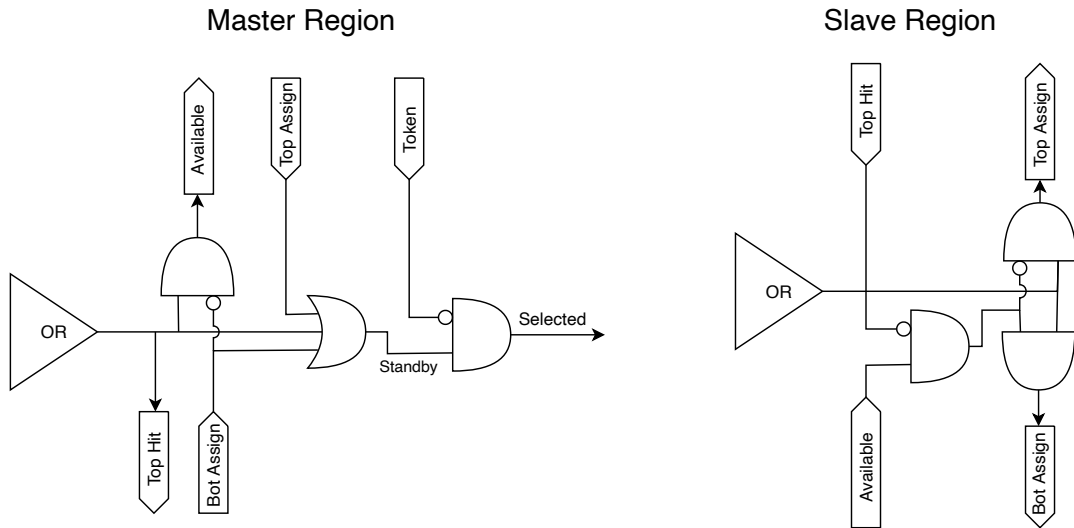


Figure 1.5

Depending on the active flags of the neighbouring Masters, the Slave bitmap is assigned to the one at the top or bottom. If both the Masters have an active flag, the Slave is assigned to the top one. In the example in figure 1.6 two Master-Slave regions are considered: the bitmaps of the Master (red colored in the example) and Slave (blue colored) are joined together within a unique data packet and a bit (green colored) is used to specify the Slave.

The data packets are transmitted to the End of Section (EoS) with a priority chain similar to what happens in TJ-Monopix1. If at least one Master set a high flag, a **Token** signal is generated and is assigned to the high priority Master in the column, together with a **Full** flag which is distributed to the active Masters in the whole column in order to deny more region to be accessed at the same time. The readout then propagates down the column from Master to Master, skipping the empty cores; the Master selected for the readout is the one with the flag high and with an input (from top) **Token** equal to 0. In the example in figure 1.7 the **Token** is propagated from the Pixel Region (PR) 10 to the PR 7. In the three readout steps the red Masters are the ones selected for the readout, while the yellow are the ones which an active flag high; gray color is used for empty regions. When a specific Master has been selected, a **Read** signal is generated both to transmit the data to the EoS and also to generate a reset for the just read pixels. Once the pixels are reset, the Master's **Full** and **Token** flags fall, and the following region which satisfies the two readout conditions explained above, becomes selected.

<sup>143</sup> The performances of the readout has been studied with simulations by the designer  
<sup>144</sup> of the chip. Random hits events with cluster size of 4 pixels on average, with a Poisso-  
<sup>145</sup> nian distribution in time and uniformly distributed on the matrix has been generated.

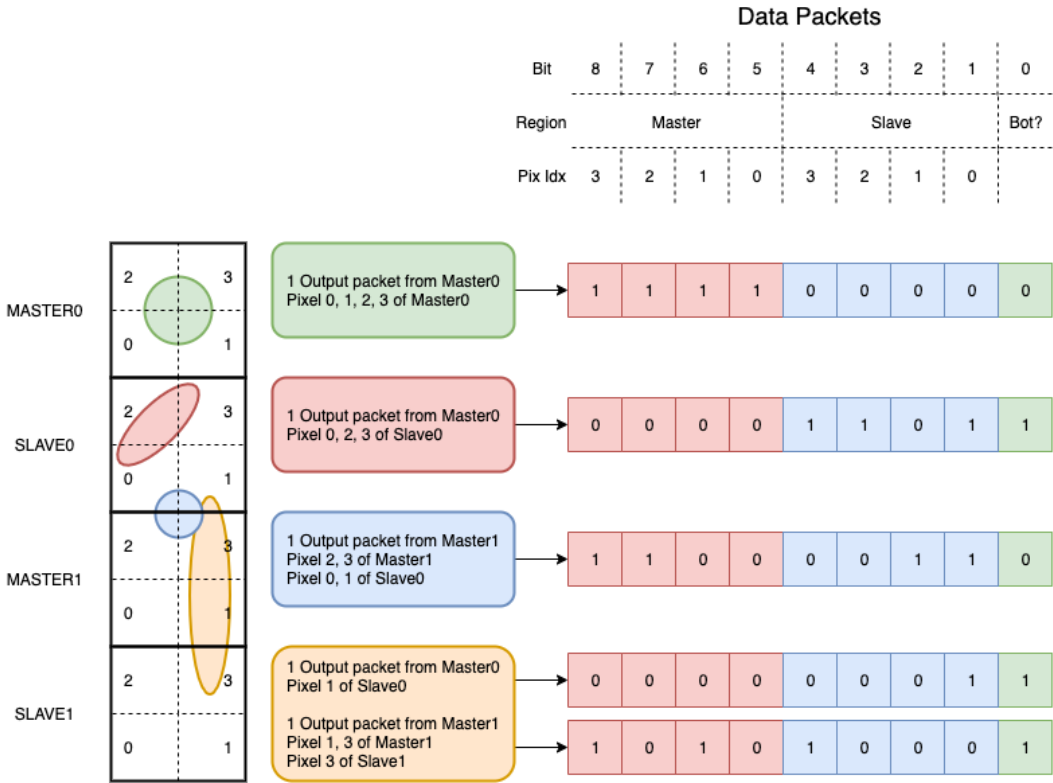


Figure 1.6: Different cluster structures and the data packet produced by them are shown in the example.

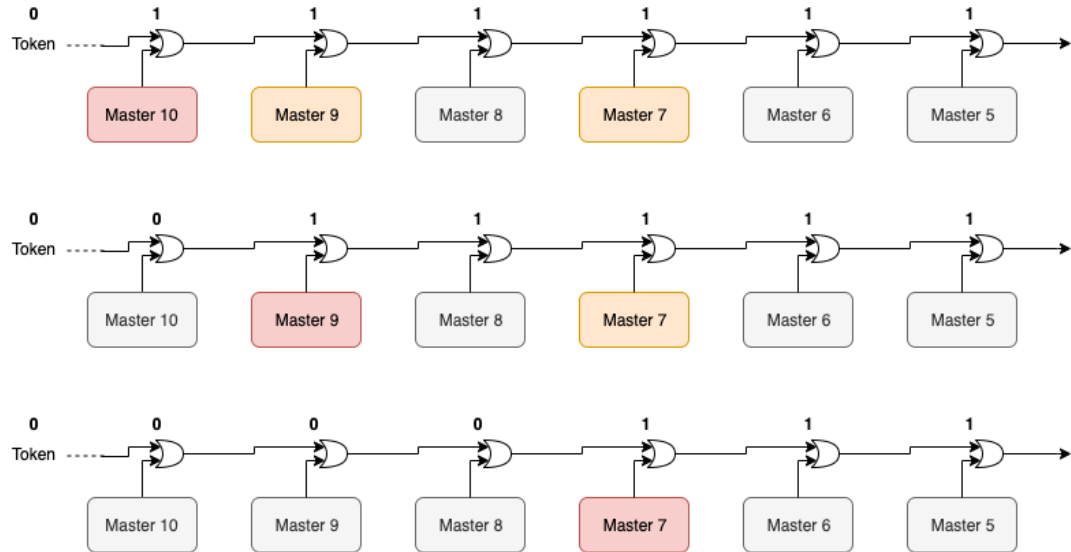


Figure 1.7

<sup>146</sup> They state that with particle hit rate of 100 MHz/cm<sup>2</sup>, considering a portion of matrix of  
<sup>147</sup> three section (512×96), the efficiency results to be 98.7%, while reducing the hit rate to  
<sup>148</sup> 80 MHz/cm<sup>2</sup> it is even higher achieving the 99.95%.

<sup>149</sup> **Chapter 2**

<sup>150</sup> **Characterization**

<sup>151</sup> Rifai il conto della lunghezza di attenuazione. Ho trovato (presentazione Luciano Mus) 29  
<sup>152</sup> um per ka e 37 um per kb.

<sup>153</sup> **2.1 TJ-Monopix1 characterization**

<sup>154</sup> **2.1.1 Threshold and noise: figure of merit for pixel detectors**

<sup>155</sup> A characterization of threshold and noise is typically necessary since these values have an  
<sup>156</sup> impact on the operating conditions and on the performance of the chips, so much that  
<sup>157</sup> the signal to threshold ratio may be considered as the figure of merit for pixel detectors  
<sup>158</sup> rather than the signal to noise ratio. The mean minimum stable threshold evolved through  
<sup>159</sup> different generation of chips: in the 1st generation it was around  $2500 \text{ e}^-$  while in the 3rd  
<sup>160</sup> (corresponding to nowadays chips) is less than  $500 \text{ e}^-$ . This allows in thinner sensors with  
<sup>161</sup> smaller signals: from  $16\,000 \text{ e}^-$  produced in  $200 \mu\text{m}$ , the signal expected moved down to  
<sup>162</sup>  $2000 \text{ e}^-$  produced in  $25 \mu\text{m}$ . In agreement with this, the threshold of TJ-Monopix1 is  
<sup>163</sup> around  $500 \text{ e}^-$ .

<sup>164</sup> Obviously the threshold has to be located between the noise peak around the baseline  
<sup>165</sup> and the signal distribution, in particular it has to be low enough to maintain a high signal  
<sup>166</sup> efficiency, but also high enough to cut the noise: for a low threshold many pixels can fire  
<sup>167</sup> at the same time and a positive feedback can set off a chain reaction eventually, causing  
<sup>168</sup> all the other pixels to fire. Thus, the noise sets a lower bound to the threshold: if an  
<sup>169</sup> occupancy  $\leq 10^{-4}$  is required, for example, a probability of firing lower than that value  
<sup>170</sup> is needed and this, assuming a gaussian noise, requires that the threshold is set at least  
<sup>171</sup>  $3.7\sigma$ , with  $\sigma$  the RMS of the noise. In this case, if the noise is  $100 \text{ e}^-$  (reasonable), the  
<sup>172</sup> threshold must be higher than  $3.7 \times 100 \text{ e}^-$ . Typically this argument sets only a minimal  
<sup>173</sup> bound to the threshold since the variation with time and from pixel to pixel have to be  
<sup>174</sup> taken into account: the temperature, the annealing (for example, the radiation damages in  
<sup>175</sup> the oxide layer causes shift of MOSFET threshold voltage) and the process parameters  
<sup>176</sup> variation across the wafer (as for example process mismatch between transistors).

<sup>177</sup> On the other hand, concerning the noise, given that the first stage of amplification is  
<sup>178</sup> the most crucial, since in the following stages the signal amplitude is high compared to  
<sup>179</sup> additional noise, it is valued at the preamplifier input node. Then, the noise is parame-  
<sup>180</sup> terized as Equivalent Noise Charge (ENC), which is defined as the ratio between the noise  
<sup>181</sup>  $N$  at the output expressed in Volt and the out voltage signal  $S$  produced by  $1 \text{ e}^-$  entering

182 in the preamplifier:

$$ENC = \frac{N_{out}[V]}{S_{out}[V/e-]} = \frac{V_{noise}^{RMS}}{G} \quad (2.1)$$

183 with G expressed in V/e-; as the gain increases, the noise reduces .

184 Considering the threshold dispersion a requirement for the ENC is:

$$ENC < \sqrt{(T/3.7)^2 - T_{RMS}^2(x) - T_{RMS}^2(t)} \quad (2.2)$$

185 where the T is the threshold set,  $T_{RMS}$  is the threshold variation during time (t) and  
186 across the matrix (x); a typical reasonable value often chosen is 5 ENC.

187 Because of the changing of the 'real' threshold, the possibility of changing and adapting  
188 the setting parameters of the FE, both in time and in space is desiderable: these parameters  
189 are usually set by Digital to Analog Converter (DAC) with a number of bit in a typical  
190 range of 3-7. Unfortunately DAC elements require a lot of space that may be not enough  
191 on the pixel area; therefore, the FE parameters are typically global, which means that they  
192 are assigned for the whole chip, or they can be assigned for regions the matrix is divided  
193 into. The former case corresponds to TJ-Monopix1's design in which 7 bits are used for  
194 a total 127-DAC possible values, while the latter corresponds to the ARCADIA-MD1's  
195 one, **where quanti bit??**. An other possibility, for example implemented in TJ-Monopix2,  
196 is allocate the space on each pixel for a subset of bits, then combinig the global threshold  
197 with a fine tuning. If so, the threshold dispersion after tuning is expected to decrease  
198 depening on the number of bits available for tuning:

$$\sigma_{THR,tuned} = \frac{\sigma_{THR}}{2^{nbit}} \quad (2.3)$$

199 where  $\sigma_{thr}$  is the RMS of the threshold spread before tuning.

200 To measure the threshold and noise of pixels a possible way is to make a scan with  
201 different known injected charge: the threshold corresponds to the value where the efficiency  
202 of the signal exceeds the 50%, and the ENC is determined from the slope at this point.  
203 Assuming a gaussian noise, e.g. a noise whose transfer function turns a voltage  $\delta$  pulse in a  
204 gaussian distribution, the efficiency of detecting the signal and the noise can be described  
205 with the function below:

$$f(x, \mu, \sigma) = \frac{1}{2} \left( 1 + erf \left( \frac{x - \mu}{\sigma\sqrt{2}} \right) \right) \quad (2.4)$$

206 where  $erf$  is the error function. Referring to 2.4 the threshold and the ENC corresponds  
207 to the  $\mu$  and  $\sigma$ .

208 I used the injection circuit available on the chip to inject 100 pulses for each input  
209 charge for a fixed threshold. The injection happens on a capacity at the input of the FE  
210 circuit, whose nominal value is 230 aF and from which the conversion factor from DAC  
211 units to electrons can be obtained: for the PMOS flavor, for example, since the DAC are  
212 biased at 1.8 V, the Least significant Bit (LSB) corresponds to a voltage of 14.7 mV from  
213 which the charge for LSB  $1.43 \text{ e-}/\text{mV}$  and the conversion factor therefore is  $20.3 \text{ e-}/\text{DAC}$ .  
214 While this value is equivalent for all the PMOS flavor, the HV flavor is expected to have a  
215 different conversion factor,  $\sim 33 \text{ e-}/\text{DAC}$ , beacuse of the different input capacity. Besides  
216 the charge, also the duration and the period of the injection pulse can be set; it is important  
217 to make the duration short enough to have the falling edge during the dead time of the  
218 pixel (in particular during the FREEZE signal) in order to avoid the undershoot, coming

	PMOS A	PMOS B	PMOS C	HV
Threshold [e <sup>-</sup> ]	401.70±0.15	400.78±0.24	539.66±0.58	403.87±0.19
Threshold dispersion [e <sup>-</sup> ]	32.90±0.11	32.97±0.17	55.54±0.42	44.67±0.15
Noise [e <sup>-</sup> ]	13.006±0.064	12.258±0.068	13.88±0.11	11.68±0.10
Noise dispersion [e <sup>-</sup> ]	1.608±0.044	1.504±0.046	1.906±0.072	1.580±0.068

Table 2.1: Mean threshold and noise parameters for all flavor and their dispersion on the matrix.

at high input charge, triggering the readout and reading spurious hits. Since the injection circuit is coupled in AC to the FE, if the falling edge of the pulse is sharp enough to produce an undershoot, this can be seen as a signal.

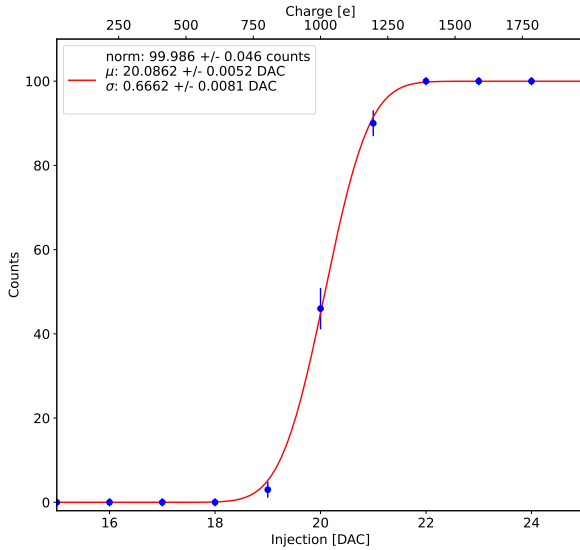


Figure 2.1: S-curve for pixel (10, 10) of the PMOS flavor (flavor B) with IDB fixed at 40 DAC. The conversion of charge injected from DAC to electrons has been performed using a nominal conversion factor of  $20.3 \text{ e}^-/\text{DAC}$  *Mi sono resa conto che l'asse superiore è sbagliato. Devo rigenerare il plot*

with IDB equal to 40 DAC

Therefore I fitted the counts detected using the function in equation 2.4. Figure 2.1 shows an example of such fit for a pixel belonging to the flavor B, while in figure 2.2 are shown the 1D and 2D distributions of the parameters found. I fitted the 1D distributions with a gaussian function to found the average and RMS of the noise and the threshold for each flavor across the matrix. The results are reported in table 2.1.

In the map at the top right panel of figure 2.2 (IDB=40 DAC) a slightly lower threshold is visible in the first biasing section (columns from 0 to 14); similar structures, but extended to the entire matrix, appear more evidently when using different IDB values. The systematic threshold variation across the biasing group has not a known motivation, but one could certainly be the transistor mismatch of the biasing DAC registers IDB and ICASN, which both adjust the effective threshold (I recall that ICASN regulate the

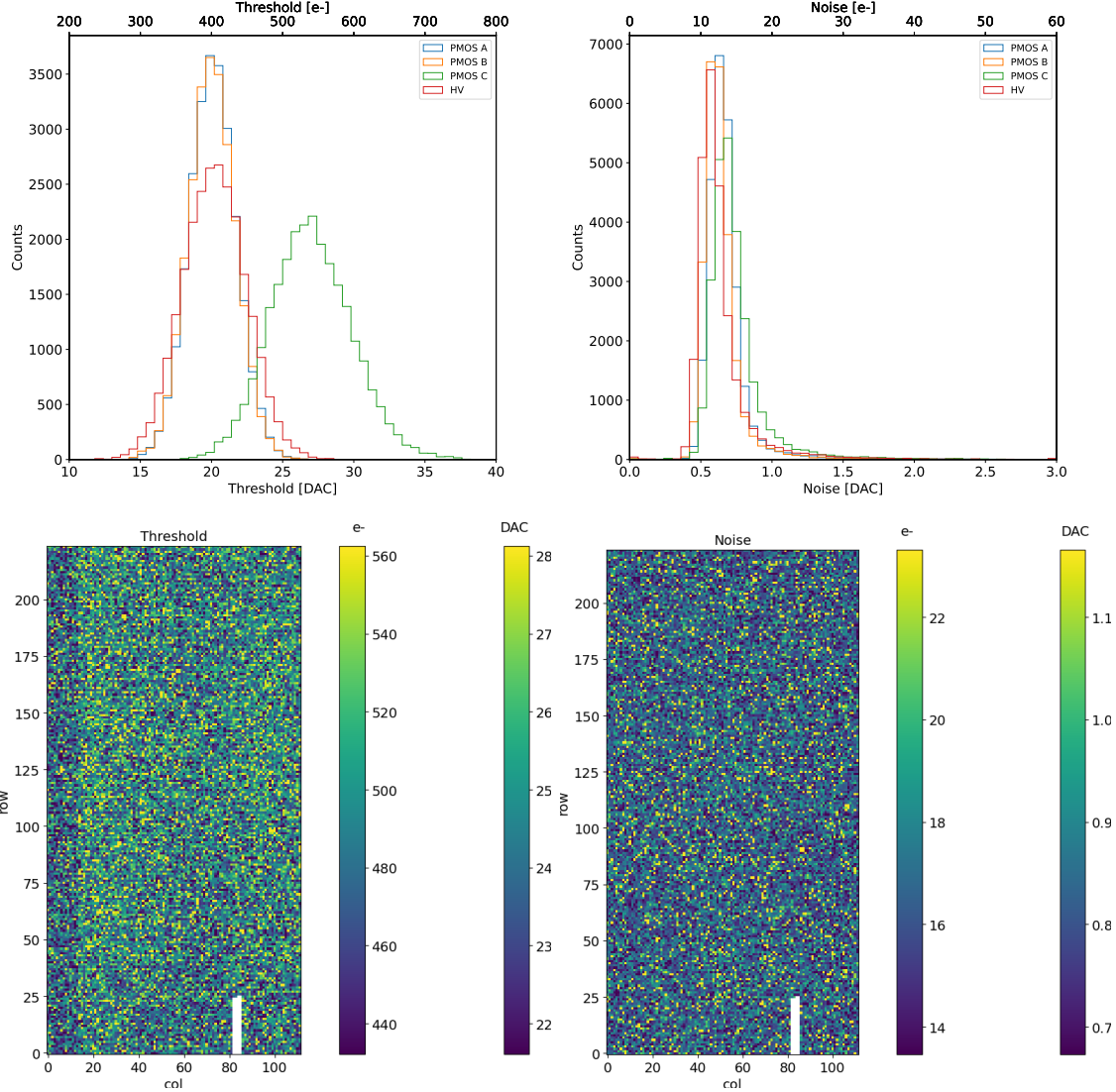


Figure 2.2: Histograms of the threshold (a) and the noise (b) found fitting the s-curve of all flavor with IDB fixed at 40 DAC. Below there are the maps of the threshold (a) and the noise (b), respectively, found fitting the s-curve with IDB fixed at 40 DAC for the PMOS flavor (B). The white pixels have the injection circuit broken.

234 baseline).

235 To verified the trend of the threshold as a function of the front end parameter IDB and  
 236 find its dynamic range, I have permormed different scans changing the FE register IDB.  
 237 For each IDB I have injected the whole matrix and search for the mean and the standard  
 238 deviation of the threshold and noise distributions. The results are shown in figure 2.3:  
 239 the blue points are the mean threhsold found whithin the matrix, while in green is shown  
 240 the width of the threshold distribution, aka the threshold dispersion. While the threshold  
 241 increases, the ENC decreases of  $\sim 4 \text{ e-}$ ,which is  $\sim 1/3$  of the noise at IDB=40 DAC.

242 Then, to evaluet the operation and the occupancy of the chip at different threshold  
 243 I have made long acquisitions of noise at different IDB and check how the number of  
 244 pixel masked changes with the threshold. The masking algorithm I have used search for  
 245 pixels with rate  $> 10 \text{ Hz}$  and mask them. With such algorithm, in our standard condition,

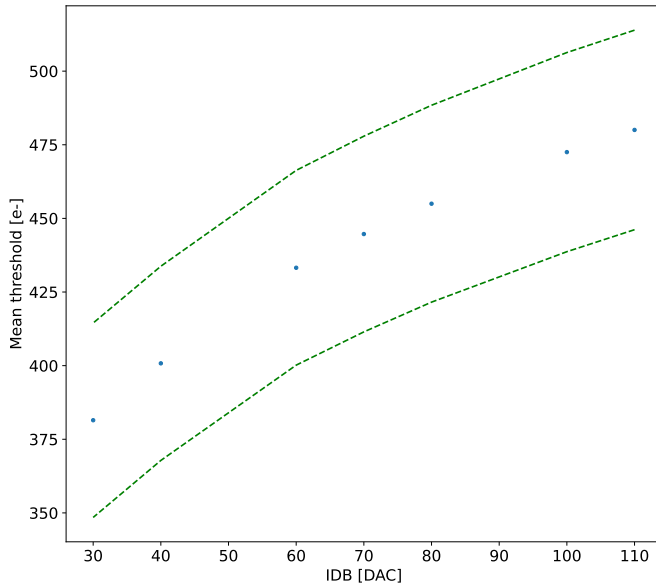


Figure 2.3: Flavor PMOS (B) with Psub-Pwell biased at -6 V. Threshold measured in electrons vs the register which sets the threshold, IDB.

246    IDB=40 DAC, a very low noise hit rate is intentionally achieved masking a dozen of pixels  
 247    of the whole flavor.

### 248    2.1.2 Linearity of the ToT

249    I have already said in chapter ?? that TJ-Monopix1 returns an output signal proportional  
 250    to the charge released by a particle in the epitaxial layer, which is the Time over Threshold;  
 251    the ToT is saved as a 6-bit variable and then has a dynamic range equal to 0-64, which  
 252    corresponds to 0  $\mu$ s to 1.6  $\mu$ s assuming a clock frequency of 40 MHz. When a pulse is longer  
 253    than 1.6  $\mu$ s the counter rolls back to zero and there is no way to distinguish that charge  
 254    from a lower one with the same ToT: that is the rollover of the ToT (2.4(a)).

255    In order to associate the ToT (in range 0-64) to the charge, a calibration of the signal  
 256    is necessary. Assuming the linearity between ToT and the charge, Q can be found:

$$Q [DAC] = \frac{(ToT [au] - offset [au])}{slope [au/DAC]} \quad (2.5)$$

257    where m and q are the fitted parameters of the calibration. It is important to keep in mind  
 258    that the main application target of TJ-Monopix1 is in the inner tracker detector of HEP  
 259    experiments, then the main feature is the efficiency, then a rough calibration of the signal  
 260    to charge is fine. The ToT information can be used both to better reconstruct the charge  
 261    deposition in cluster in order to improve the track resolution, and for particle identification,  
 262    especially for low momentum particles which do not reach the proper detectors.

263    The study of the output signal is made possible via the injection: since the pulses  
 264    are triangular, the ToT is expected to be almost therefore, to prevent th linear. To verify  
 265    this statement and study the deviations from linearity I fitted the ToT versus the charge  
 266    injected for all the pixels within the matrix. In figure 2.4(b) there is an example of fit

for a pixel belonging to the flavor B, while in figure 2.5 there are the histograms and the maps of the parameters of the line-fit for all flavors with IDB fixed at 40 DAC. Here again a difference among the biasing section appears: since the slope of the ToT is related with the gain of the preamplifier (increasing the gain also increases the ToT), the mismatch is probably due to the transistor contributing to the amplification stage.

I fitted the average ToT of all the pulses recorded as a function of the pulse amplitude; data affected by rollover have been removed in order to avoid introducing a bias in the mean values. In figure 2.4 (b) are shown both the fits with a line (red) and with a second order polynomial (green): at the bounds of the ToT range values deviate from the line model. Since the deviation is lower than 1% and it only interests the region near the 0 and the 64, in first approximation it is negligible.

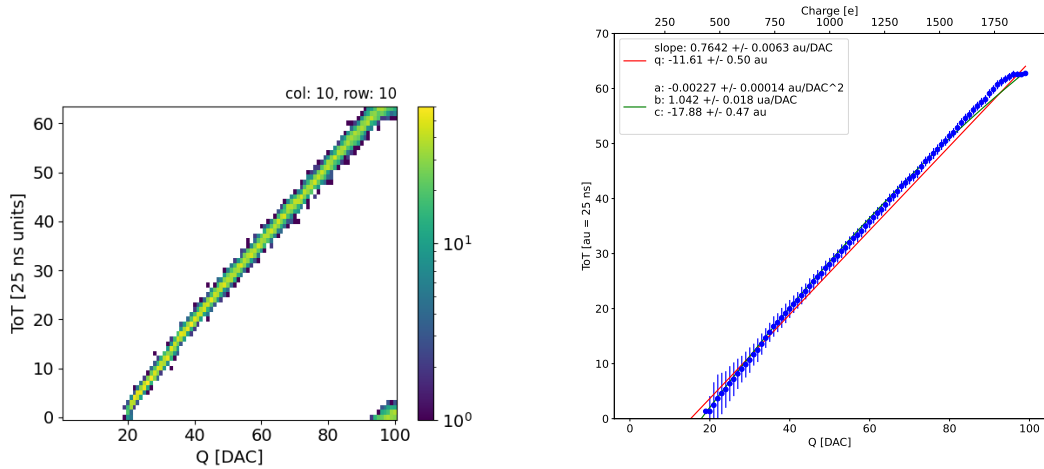


Figure 2.4: The figures refer to pixel (10,10) of the PMOS-reset flavor B with IDB fixed at 40 DAC. (a) Histogram of the injection pulses: the ToT is in range 0-64 since it is represented by 6 bit, so when achieving the 64 it rolls over back to the zero. (b) Mean ToT vs the charge: the mean has been calculated cutted the rolling hits.

### 2.1.3 Calibration of the ToT

Finding a calibration for the ToT means defining a way to pass from the ToT values (0-64 clock counts) to a spectrum expressed in electrons collected. The principles of the calibration are the following: the ToT in clock counts maps (eq.2.1.2) a DAC range between the threshold and a value which depends on the pixel and generally is around 90-100 DAC. Assuming that a 0 DAC signal corresponds to 0 e<sup>-</sup>, if another reference point is fixed, a linear calibration function can be defined. After the calibration the ToT goes to map a charge range between the threshold and  $Q_{max}$  which is a function of the pixel and is around 2 ke<sup>-</sup>.

Moreover, considering that the charge injected in the FE goes to fill a capacitor C which is different from pixel to pixel, the true charge injected does not correspond to what expected assuming C equal to 230 aF, which is the nominal value. Accordingly to that, a measurement of this value provides both an absolute calibration of C and a conversion factor K to have a correspondence of the DAC signal in electrons. K and C are defined

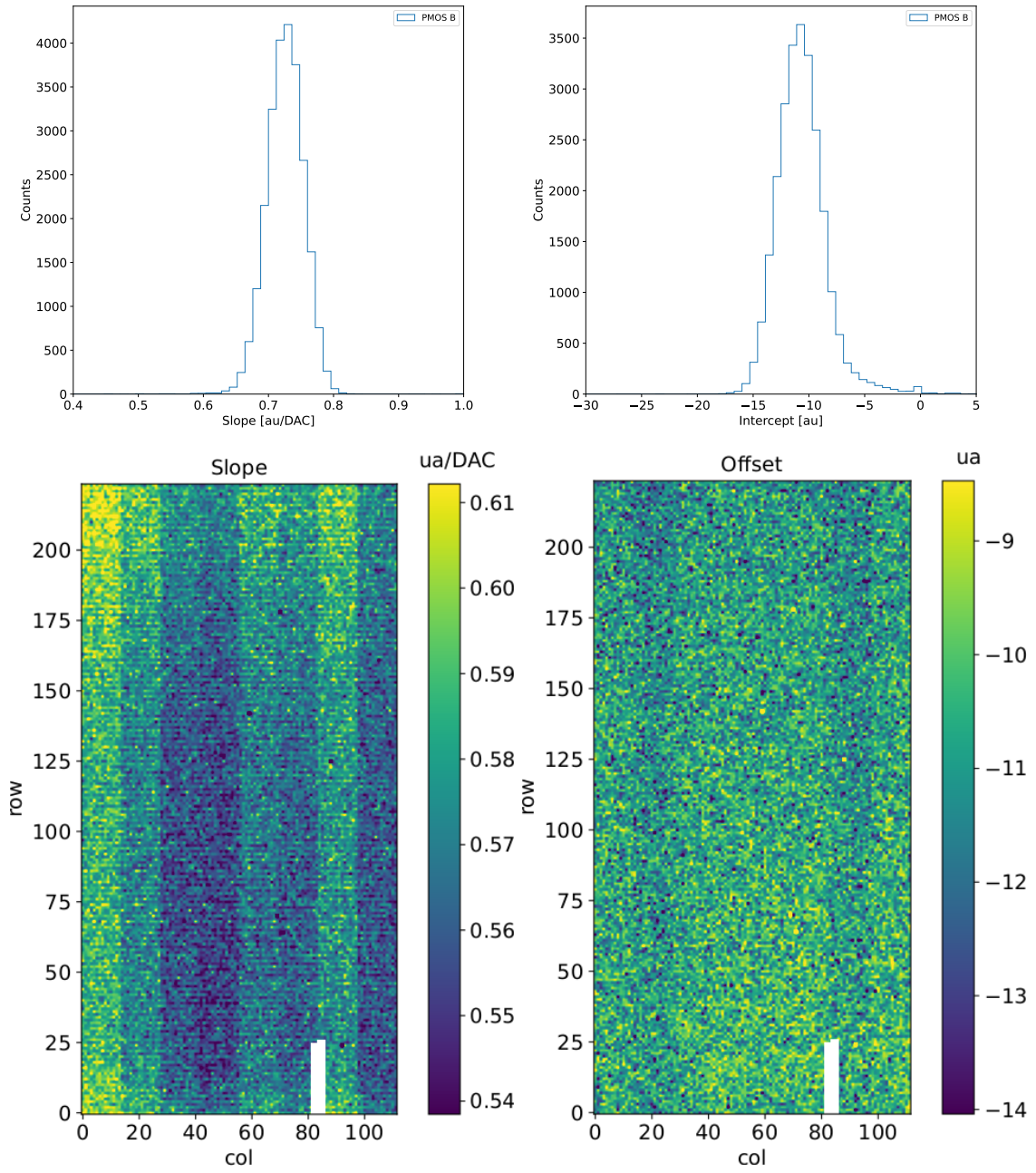


Figure 2.5: Histograms of the calibration parameters, slope (a) and offset (b), found fitting the ToT with a line, for the flavor B and with IDB fixed at 40 DAC. Maps of the calibration parameters, slope (a) and offset (b), found fitting the ToT with a line, with IDB fixed at 40 DAC.

292 respectively as:

$$K [e^- / DAC] = \frac{1616 [e^-]}{Q [DAC]} \quad (2.6)$$

293

$$C [F] = [e^- / DAC] \frac{1.6 \cdot 10^{-19} [C]}{14.7 [mV]} \quad (2.7)$$

294 where K is expected to be  $20 e^- / DAC$ , assuming the nominal value of C equal to  $230 aF$ ,  
295 and where 1616 is the expected number of electrons produced by the calibration source

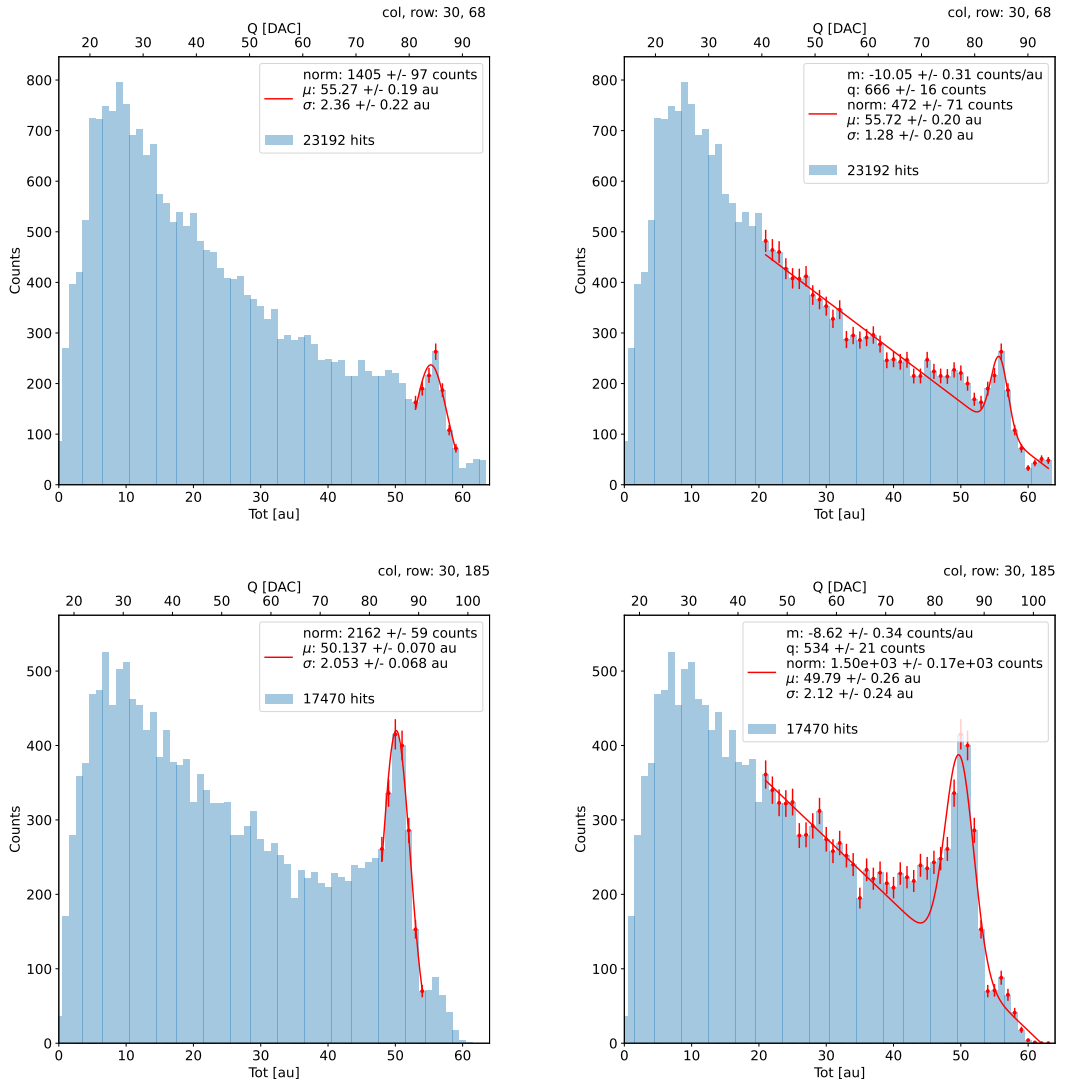


Figure 2.6: due pixel per far vedere la differenza tra i fit. Sottolinea che in rosso ci sono i bin fittati. La doppia scala utilizza le info trovate nel paragrafo precedente per il dato pixel in questione. Per avere una corrispondenza grezza in elettroni basta moltiplicare per 20 e- / dac.

used, Fe55. Fe55 is an extremely important radionuclide in the calibration of X-ray spectrometers, proportional counter and scintillator detector since it emits two X-photons during the electron capture decay: the first one ( $K_{\alpha}$ ) at 5.9 keV and the second one ( $K_{\beta}$ ) at 6.5 keV. The  $K_{\alpha}$  photon, which does photoelectric effect in silicon, has an absorption length  $\lambda=7 \mu\text{m}$  to  $8 \mu\text{m}$ , and the probability of being absorbed in the  $25 \mu\text{m}$  thick epitaxial layer is  $\sim 0.95\%$ . The electron emitted has an energy equal to the photon, so recalling that the mean energy needed to produce a couple electron-vacuum is 3.65 eV, the signal produced by the Fe55 source is expected to be  $1616 \text{ e-}$ . In figures 2.6 are shown two histograms of the ToT spectrum of the Fe55 source for two different pixels. The peak on the right corresponds to the events with complete absorption of the charge in the depleted region, while the long tail on the left to all the events with partial absorption due to charge sharing among neighbors pixels. In order to reduce the consistent charge sharing, the pixel dimension in TJ-Monopix2 has been reduced down to  $30 \times 30 \mu\text{m}^2$ . The events on the right

309 side of the peak, instead, corresponds to the  $K_\beta$  photons. Looking at the histograms for  
 310 pixel (30, 185) and (30, 69) a significant difference in the peak to tail ratio leaps out, which  
 311 can be related with the position of the pixel in the matrix. In particular, because of a  
 312 different charge collection property, pixels in the upper part of the matrix (rows 112-224)  
 313 have a more prominent peak, while in pixels in the lower part (rows 0-111) there is a  
 314 higher partial absorption. Indeed, as discussed in section ??, there is a distinction in the  
 315 structure of the low dose-epi layer among the rows, in particular pixels in rows 112-224,  
 316 which have a RDPW, are supposed to have a higher efficiency in the pixel corner.

317 For the calibration I needed to establish the peak position; to do that I fitted the ToT  
 318 histogram of each pixel. I tested two different fit functions:

$$f(x, N, \mu, \sigma) = \frac{N}{\sigma\sqrt{2\pi}} e^{-\frac{1}{2}(\frac{(x-\mu)}{\sigma})^2} \quad (2.8)$$

319

$$f(x, m, q, N, \mu, \sigma) = m x + q + \frac{N}{\sigma\sqrt{2\pi}} e^{-\frac{1}{2}(\frac{(x-\mu)}{\sigma})^2} \quad (2.9)$$

The additional linear term in equation 2.9 is meant to model the tail due to incomplete

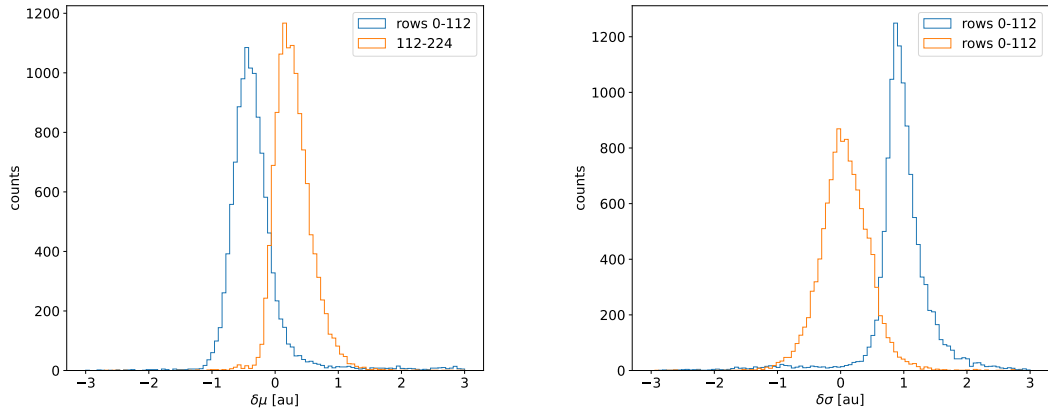


Figure 2.7: Difference between the parameters  $\mu$  and  $\sigma$  obtained with the gaussian fit and those obtained with a gaussian plus a line. When  $\mu < 0$  the fit with function 2.8 is generally worse (the peak is shifted to the left); when  $\sigma < 0$ , the fit with 2.9 is worse (larger sigma).

320

321 charge collection and prevent it from introducing a bias in the fitted peak position.

322 For this reason, when fitting with eq.2.9, I selected a larger region compared to the  
 323 fit with eq.2.8, for which I used only a small reagion around the peak. The optimal fit  
 324 region was chosen in both cases through an iterative routine: for the fit with eq.2.9 it  
 325 starts from an interval including all the pixels above 20 DAC and progressively reduces it  
 326 by increasing the left boundary; for the fit with eq.2.8, it starts from an interval of 5 bins  
 327 around the expected peak position and reduces the interval of 1 bin at each iteration.

328 Even if the difference in the peak position between the two fit strategies is not really  
 329 relevant for the purpose of the calibration, being of the order of 0.8-1.5% (2.7),it still  
 330 introduces a systematic bias towards lower values due to the contribution of the tail.  
 331 Indeed, we know that the sharp edge on the right must correspond to the case of complete  
 332 absorption of the photon, so that, in general, the closest to this feature is the fitted peak  
 333 position, the better the fit is. A poor fit tends also to overestimate the peak width. Even

334 looking at the  $\chi^2$ , the fit function 2.8 seems to be the better choice, except for a sample  
 335 of pixels in the lower part of the matrix, the one with lower efficiency.

336 The resolution of the detector, which is expected to be determined by the statistical  
 337 fluctuations in the number of charge carriers generated in the detector as well as by the  
 338 ENC, can be compared to the observed Fe55 peak width. Ideally:

$$\sigma_{Fe} = \sqrt{ENC^2 + F \times N} \quad (2.10)$$

339 Since the number of e/h pairs produced in the sensor is 1616, recalling that F for a silicon  
 340 detector is 0.115 and that the ENC measured with the injection is  $12\text{e-}$ , the  $\sigma_{Fe}$  is  
 341 expected to be  $\sim 18\text{e-}$ . Looking at figure 2.8 the resolution achieved with the Fe55 source  
 342 seems to be much higher. A contribution we have not taken into account but is certainly  
 343 relevant is the systematic overestimation of the standard deviation of the Fe55 peak: this,  
 344 as I already explained, is principally due to the high background of incomplete charge  
 345 collection, which broadens the fitted peak.

346 2D maps of the value of the capacity and of the conversion factor found are shown in  
 347 2.9. The evident stripe-structure in the matrix shows an evident correlation among the  
 348 same row; the same structure, which is also visible in the slope map of the calibration of  
 the ToT (fig.1.3), may be related with the structure of the bias lines.

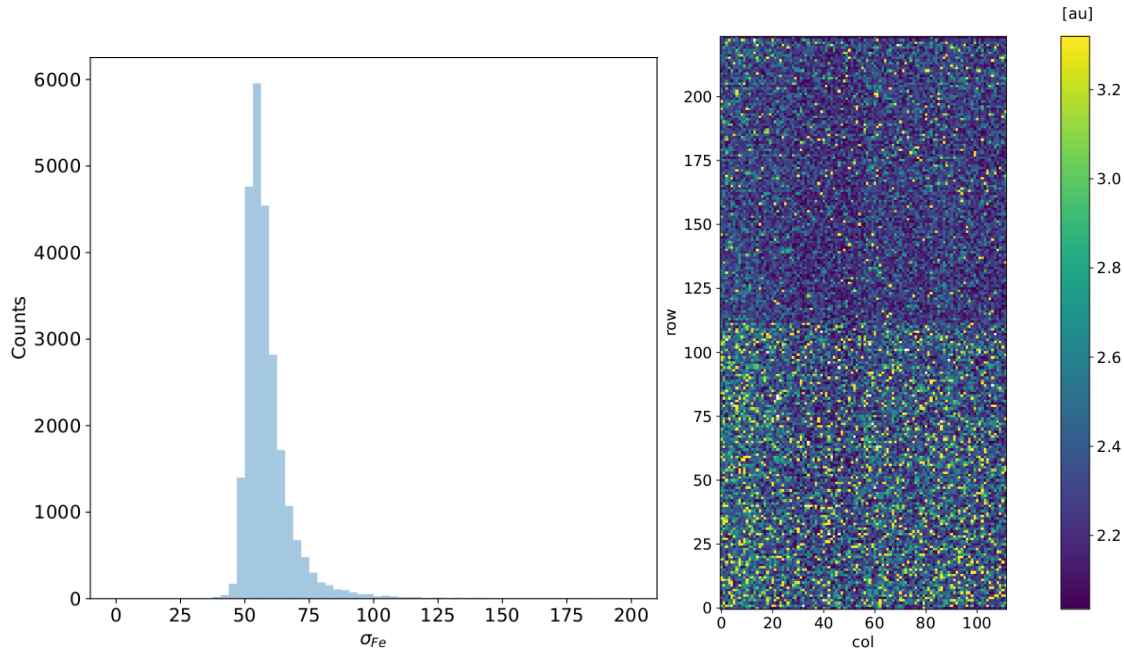


Figure 2.8: Histogram (a) and map (b) of the fitted Fe55 peak width.

349

### 350 HV flavor calibration

351 An attempt of calibrating the HV flavor, which is the most different from the PMOS B  
 352 flavor, has been performed; however, because of the loss of signal caused by the higher  
 353 capacity, we have been unable to identify the Fe55 peak in every FE and bias configuration.  
 354 An example of Fe55 spectrum collected with the HV flavor is shown in figure 2.10.

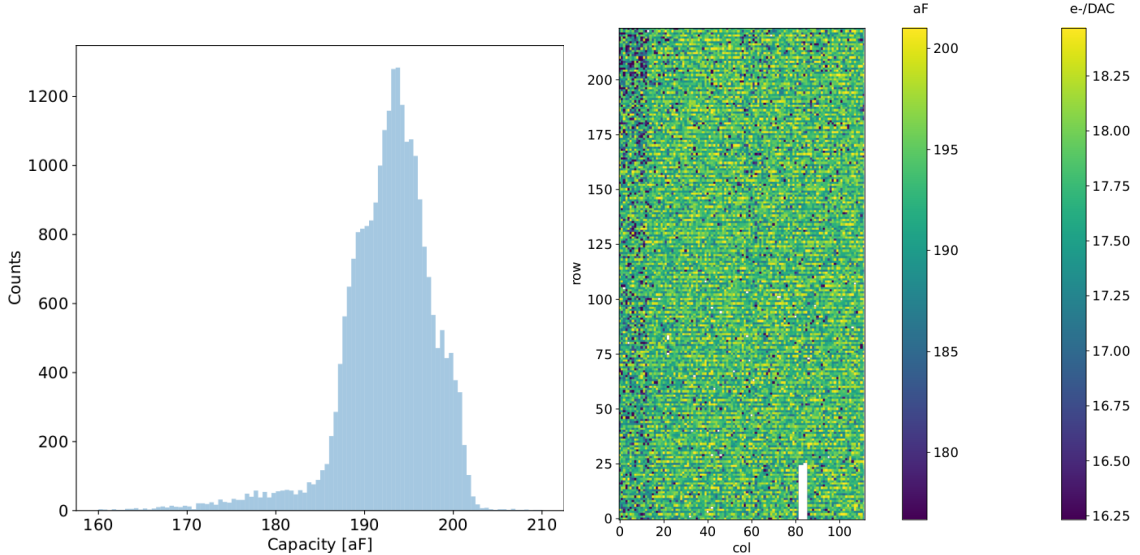


Figure 2.9: Histogram (a) and map (b) of the calibrated capacity of the injection circuit.

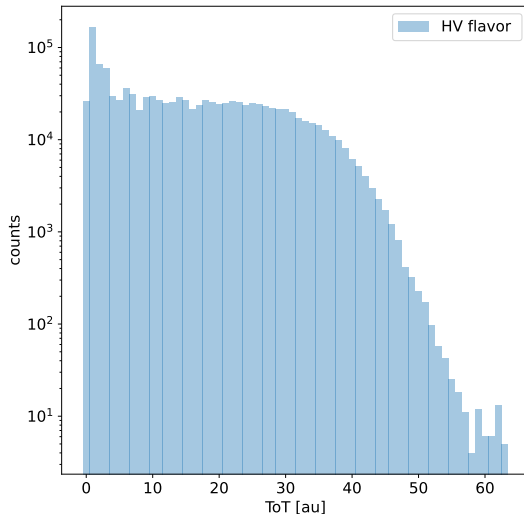


Figure 2.10: Fe55 spectrum with the HV flavor

#### 355 2.1.4 Changing the bias

356 In order to study the behavior of the sensor as a function of the bias, I performed several  
 357 injection scans in different configurations. Indeed, the thickness of the depletion region has  
 358 to be considered an important parameters affecting the signal efficiency, and in particular  
 359 it affects the charge released by a particle which crosses the sensor (since the signal is  
 360 proportional to the thickness of the epitaxial layer). The measured output voltage ampli-  
 361 tude and gain in the case of the PMOS and HV flavours are shown in figure 2.11 Given  
 362 that the chip under examination has a gap in the low dose epi-layer, we were not able to  
 363 change independently the bias of the substrate (PSUB) and of the p-well (PWELL), but  
 364 they must be kept at the same value, differently from other chips of the same submission.  
 365 Lowering the bias, the depletion region is expected to narrow and the efficiency to reduce,

	-6 V	-3 V	0 V
Threshold [DAC]	$20.0 \pm 1.6$	$21.0 \pm 1.6$	$24.5 \pm 1.8$
Noise [DAC]	$0.613 \pm 0.075$	$0.625 \pm 0.078$	$0.822 \pm 0.098$
Slope [au/DAC]	$0.726 \pm 0.027$	$0.707 \pm 0.028$	$0.573 \pm 0.021$
Offset [au]	$-10.8 \pm 1.9$	$-11.2 \pm 1.8$	$-11.1 \pm 1.5$

Table 2.2: The errors are the standard deviations of the corresponding distributions. The conversion factor from DAC to electrons is  $\sim 20 \text{ e}^-/\text{DAC}$ .

366 especially in the pixel corner, thus raising the threshold and the noise and decreasing the slope as a consequence of the reduction in the gain.

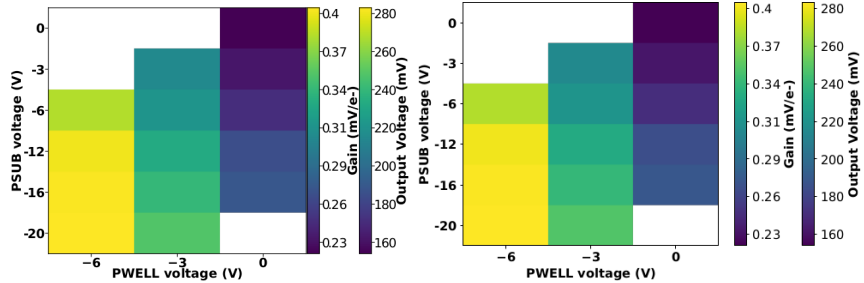


Figure 2.11: Output voltage amplitude and gain with respect to the p-well and p-substrate voltage in the case of the PMOS reset front-end (B)

367  
368 In order to test the behavior of the chip when not completely depleted, I have performed  
369 an injection scan with PSUB/PWELL bias at 0 V, -3 V and -6 V (results in tab.2.2), and  
370 some acquisitions with the Fe55 source (fig. 2.12). There are reported the values of the  
371  $K_\alpha$  peak position, the normalization of the events above the peak and the rate, everything  
372 has been normalized to the value at the reference condition, which is with PSUB/PWELL  
373 at -6 V.

### 374 2.1.5 Measurements with radioactive sources

375 In order to completely validate the operation of the whole sensor<sup>1</sup>, I have performed several  
376 acquisitions with radioactive sources, specifically Fe55 and Sr90Y, which is a  $\beta^-$  emettitor  
377 with electron endpoint at 2.2 MeV, and cosmic rays. I used the data collected with Sr90  
378 and cosmic rays, to study charge sharing and events with more than one hit.

379 I define *cluster* the ensamble of all the hits with the same timestamp. This is obviously  
380 a coarse requirement, but it gave me the opportunity of using a simple and fast clustering  
381 algorithm, which is fine when the random coincidence probability is neglibile. Defining  
382  $R_1$  and  $R_2$  as the two events rate, and  $\tau$  as the dead time of the detector, the random  
383 coincidence rate can be found:

$$R_{coinc} = R_1 \times R_2 \times \tau \quad (2.11)$$

384 As I am going to prove in the next section, the dead time strictly depends on the occupancy  
385 of the matrix, even though we can assume a dead time of  $\sim 1 \mu\text{m}$ , which corresponds to

<sup>1</sup>As I will discuss in chapter 3.2 these measurements serves also as a reference for the spectrum observed at the test beam

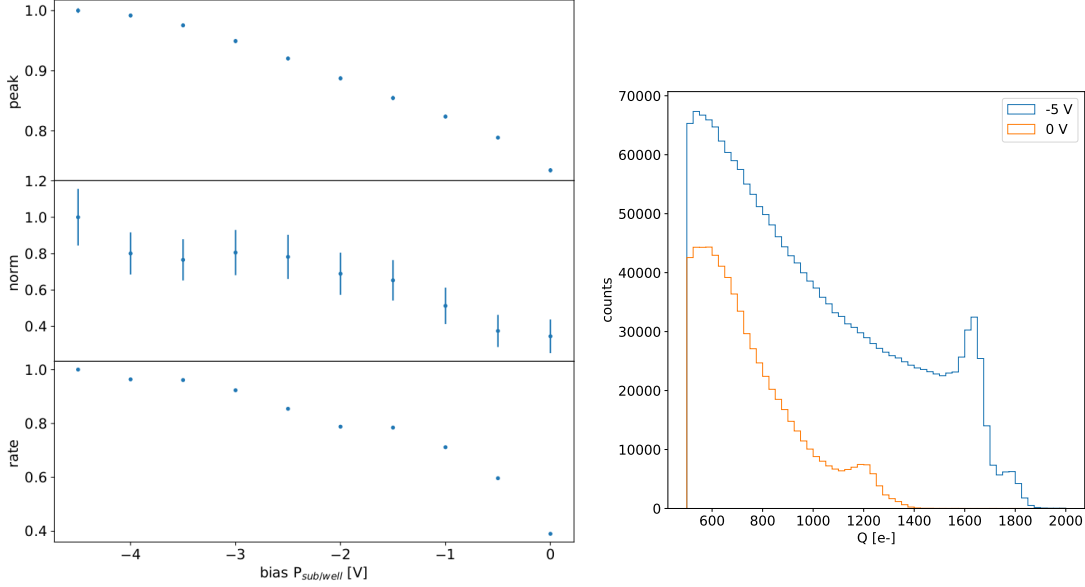


Figure 2.12: (a) Peak position, peak amplitude and rate as a function of the bias. Since during the collection of the whole data the source has been moved, it is not guaranteed that it has always had a repositioning in the same exactly place, then small the fluctuation of the rate along the decreasing trend are acceptable. The peak position and amplitude are estimated by fitting the spectrum with a gaussian in the region around the peak. (b) Fe55 spectrum at different  $P_{sub/well}$  bias. The ToT values have been calibrated as explained in section. 2.1.3.

386 the mean dead time per pixel. However, if in an event a particle hits two different pixels  
 387 producing a cluster, the total dead time simply doubles. Since the measured rate on the  
 388 whole matrix of noise, Fe55, Sr90 and cosmic rays are  $\sim$ Hz, 3.3 kHz, 40 Hz and  $\sim$ 10 mHz<sup>2</sup>,  
 389 the random coincidence probability are negligible except the one of two Fe55 events, which  
 390 is 11 Hz.

391 In figure 2.13 I report the histograms of the number of pixels in the cluster and of the  
 392 dimension of clusters, defined in terms of the max and min coordinates on the matrix as:

$$d = \sqrt{(y_{max} - y_{min})^2 + (x_{max} - x_{min})^2} \quad (2.12)$$

393 Looking at the shape of the histogram of the dimension, generally the Sr90 and the  
 394 cosmic rays produce bigger clusters and hit a higher number of pixels, a trend that can  
 395 be explained considering that the Fe55 photoelectron is much less energetic than the Sr90  
 396 electron and cosmic rays. Below I have also attached a sample of hitmap of events produced  
 397 by the three different sources (fig.2.14, 2.15).

398 In figures 2.18, 2.19, 2.21 are shown the distributions per different cluster dimension  
 399 events, of the charge collected by a single pixel (figures on the left) and the charge collected  
 400 by summing the charge collected by the pixels within the cluster (figures on the right).  
 401 Since the noise rate is comparable with the cosmic rays and Sr90 ones, I have removed the  
 402 single pixel events which are separately shown in figure 2.17; despite we cannot identify  
 403 and selecting only the noise events, these distributions, and especially the cosmic rays  
 404 one, are expected to be mostly populated by noise events. The distributions have a peak

<sup>2</sup>The cosmic rays rate at the sea level is expected to be  $\sim$ 1/cm<sup>2</sup>/s

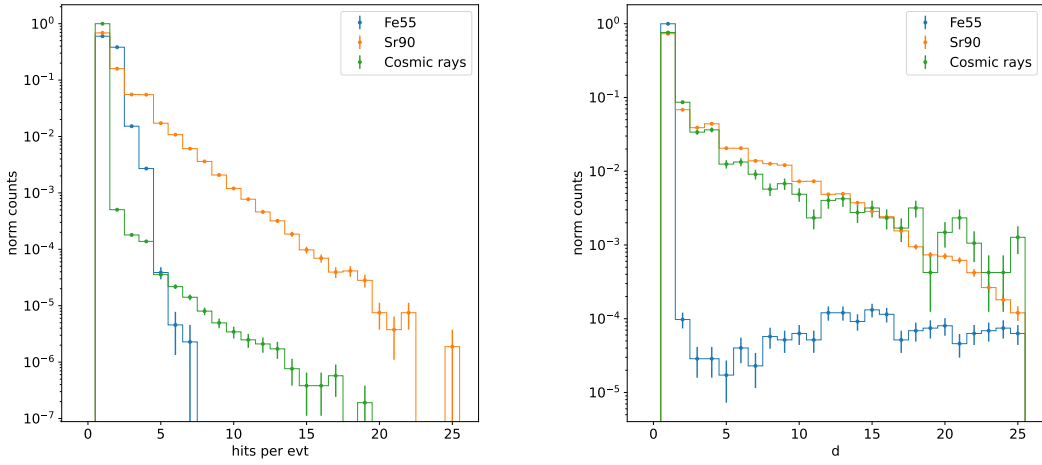


Figure 2.13: (a) Distribution of the number of hits per event with different sources. (b) Dimension of cluster defined as eq.2.1.5. Compared with the Sr90 and the cosmic rays, the Fe55 d distribution is characterized by a clear discontinuity in the cluster dimension. The very thin peak around 0 corresponds to the effective cluster, while the long tail at bigger cluster d is principally made of random coincidence.

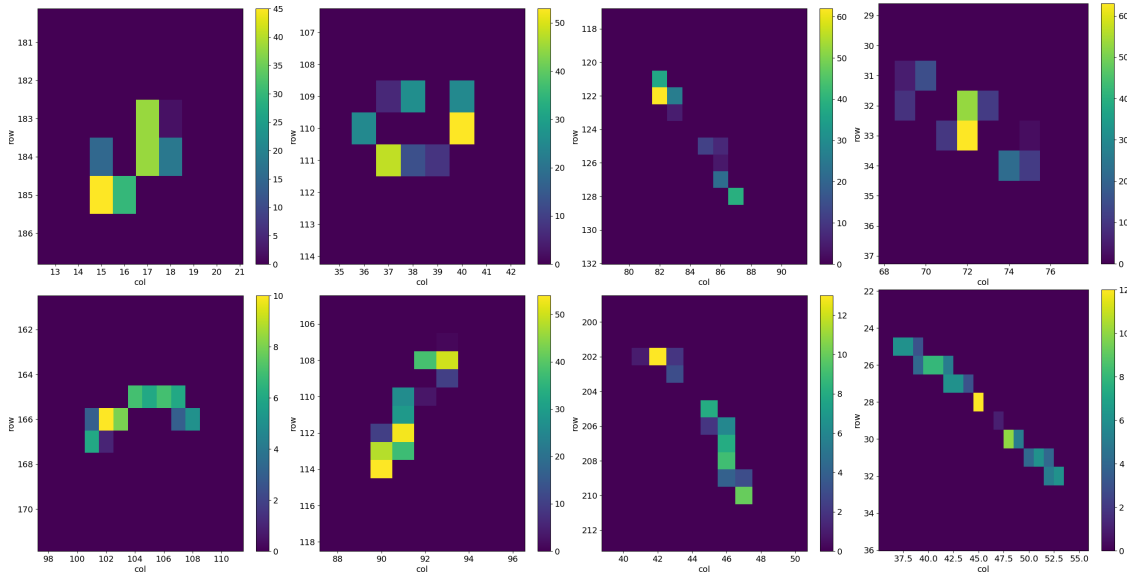


Figure 2.14: 2D histograms of the ToT in different events in an acquisition of cosmic rays.

405 around the threshold, which is compatible with the fact that the noise events typically  
406 have a low ToT.

407 Looking at the spectra of Sr90 instead (fig:2.19), the maximum of the distribution of  
408 the cluster charge seems to follow a linear dependence on the number of pixels hit (tab.2.3);  
409 this can be accepted as a first approximation considering that the pitch ( $36 \mu\text{m}$  and  $40 \mu\text{m}$ )  
410 depending on the direction, and the epitaxial layer thickness ( $25\text{-}30 \mu\text{m}$ ) are comparable.  
411 However a more accurate model which takes into account the impact angle of the particle  
412 should be developed for a more precise comparison. The charge per length covered  $Q/l$   
413 released by a particle which crosses more pixels and is not completely absorbed in the

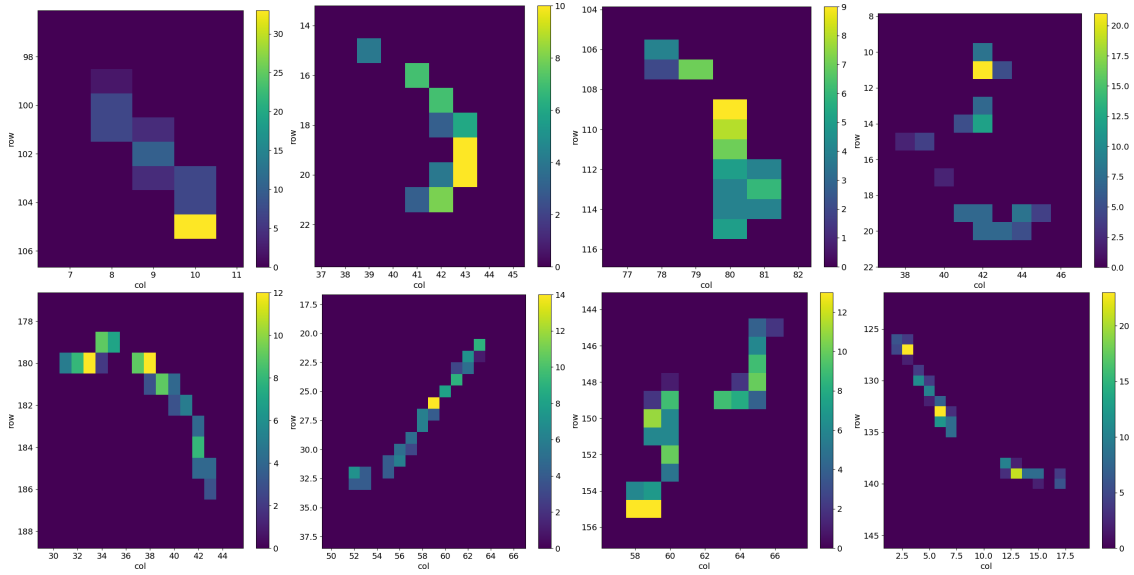


Figure 2.15: 2D histograms of the ToT in different events in an aquistion of Sr90.

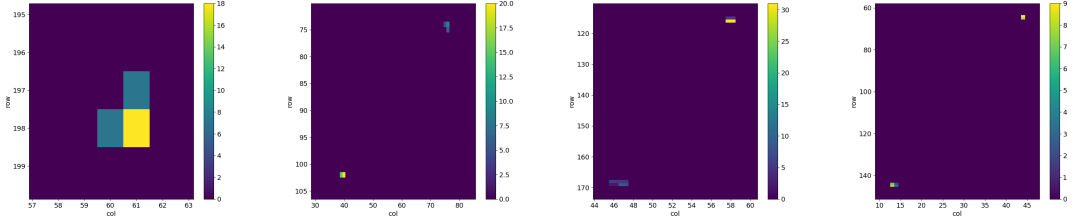


Figure 2.16: 2D histograms of the ToT in different events in an aquistion of Fe55

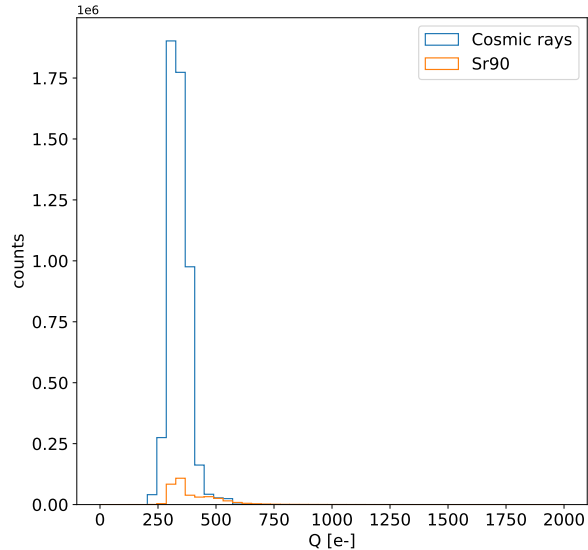


Figure 2.17: Histograms of the charge released in the pixels in events in which only a single pixel turns on.

Pixel per evt	Measured [e-]
2	$950 \pm 30$
3	$1450 \pm 30$
4	$2050 \pm 30$
5	$2450 \pm 30$

Table 2.3: Position of the maximum of the distributions in figure 2.19(b) of the summed charge released in the clusters depending on the number of pixel in the cluster.

<sup>414</sup> sensor (fig.??) can be described by the following relation. Considering that:

$$l = \frac{t}{\cos(\lambda)} = \frac{t}{\sqrt{1 + tg^2\lambda}} = \frac{t}{\sqrt{1 + (x/t)^2}} \quad (2.13)$$

<sup>415</sup> it can be expressed as:

$$\frac{Q}{l} = \frac{Q}{t} \sqrt{1 + (n - 1)^2 p^2 / t^2} \quad (2.14)$$

<sup>416</sup> where  $p/t$  is the ratio between the pitch and the epitaxial layer thickness, and then it  
<sup>417</sup> is different in the x and y directions ( $40 \mu\text{m}$  and  $36 \mu\text{m}$  respectively). Taking as value of  
<sup>418</sup>  $p/t$  1.52, which is the mean on the two axis, the value of  $Q/l$  expected by the scaling  
<sup>419</sup> relation and the charge actually measured in the acquisition with the Sr90 are illustrated  
<sup>420</sup> in table 2.3; because of the decision of cutting the single pixel events in order to have  
<sup>421</sup> a clean sample, the expected value has been obtained by the two hits cluster dividing  
<sup>422</sup> the charge by 2. By the inversion of the formula ??, the single pixel charge is then  
<sup>423</sup> expected to be 522 e-. FORSE DATO CHE LA MASSIMA CARICA RILASCIATA  
<sup>424</sup> SCALA LINEARMENTE CON IL NUMERO DI PIXEL NON SCRIVEREI QUESTA  
<sup>425</sup> COSA? O MAGARI LA METTO COME CORREZIONE? The measured value has been  
<sup>426</sup> obtained by the maximum of the distributions in the left plots in ??

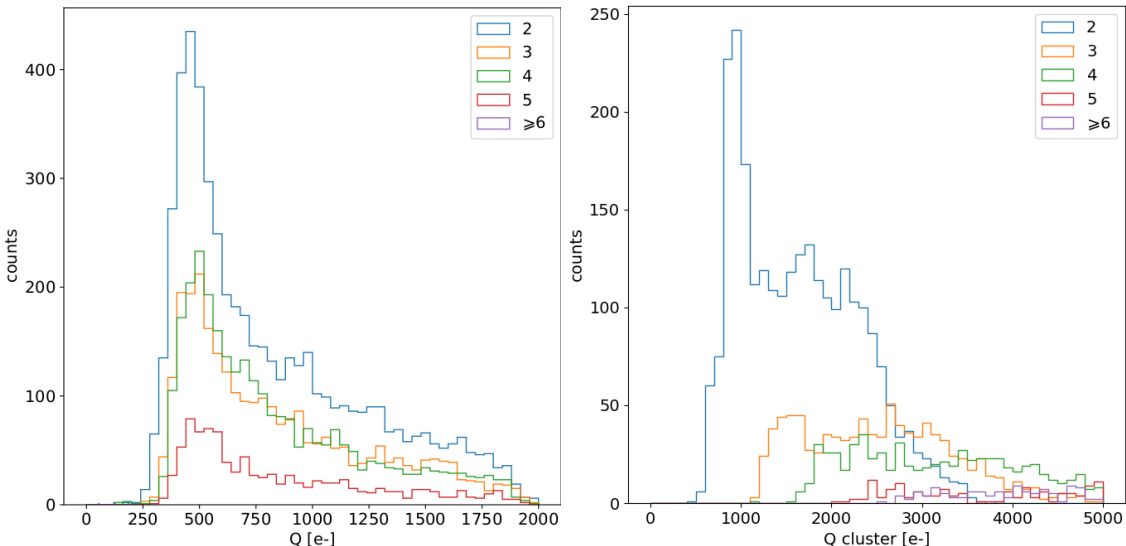


Figure 2.18: Acquisition of cosmic rays with IDB=40 DAC

<sup>427</sup> Regarding the Fe55, the bump in the cluster spectrum at  $\sim 1616 \text{ e-}$  corresponds to  
<sup>428</sup> photons which had converted at the boundary of nearby pixels thus sharing their charge  
<sup>429</sup> among them. Starting from 4-pixels clusters the peak moves to the right: this is due to

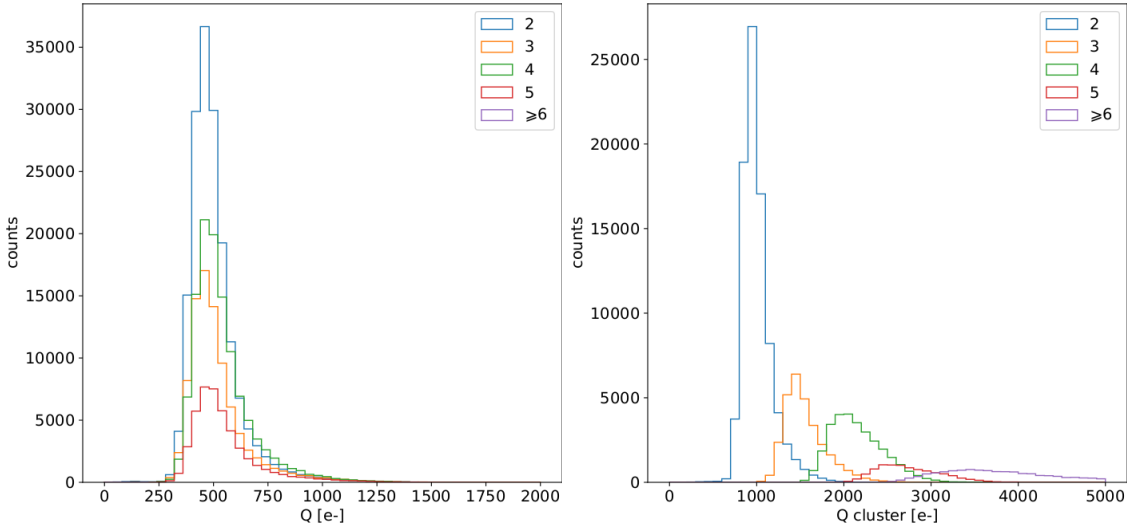


Figure 2.19: Acquisition of Sr90 with IDB=40 DAC

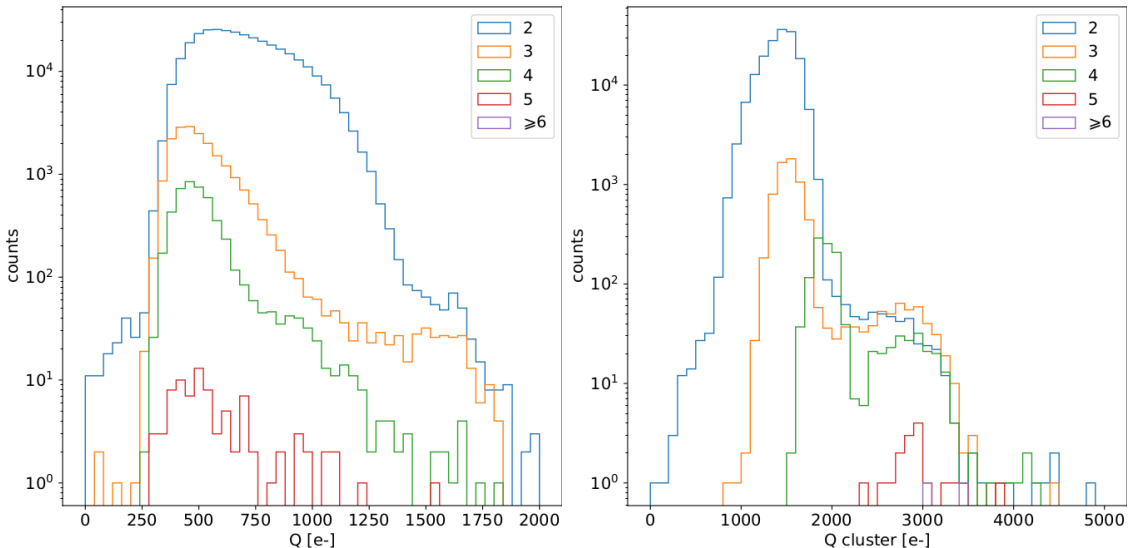


Figure 2.20: Acquisitions with radioactive source and cosmic rays at IDB=40 DAC.

Figure 2.21: Acquisition of Fe55 with IDB=40 DAC

the fact that the cluster with more than 3 pixels are principally random coincidence events Fe55-Fe55 or Fe55-noise. Recalling that the noise typically just exceeds the threshold and then has low ToT, the peak position in the spectrum 1.3 of 4-pixel cluster can be explained admitting that one of the four pixel is a noise signal. The shoulder on the right, instead, which have an edge at about 3200 e<sup>-</sup> corresponds to the events with coincidence of two photons. Looking at the charge on the single pixel spectrum (fig.1.3), instead, a small bump can be seen around 1616 e<sup>-</sup>: these events correspond to photons which released almost all the charge on one pixel.

### 2.1.6 Dead time measurements

The hit loss is due to analog and digital pile up: the first one occurs when a new hit arrives during the pre-amplifier response, the second instead when the hit arrives while

441 the information of the previous hit has not yet been transferred to the periphery. Since the  
 442 pre-amplifier response has a characteristic time  $\sim$ ToT, the dead time  $\tau_a$  introduced by it  
 443 will be at most 1.6  $\mu$ s; using the IRESET and VRESET FE parameters the reset time can  
 444 be lowered down, but as explained in section ?? it must be longer than the preamplifier  
 445 characteristics time in order to not cut the signal. Regarding the latter contribution instead,  
 446 since only one hit at a time can be stored on the pixel's RAM, until the data have completed  
 447 the path to get out, the pixel is paralyzed. Moreover since there is no storage memory  
 448 included on TJ-Monopix1 prototypes, the digital dead time  $\tau_d$  almost corresponds to the  
 449 time needed to trasmit the data-packets off-chip.

450 The exportation of data from pixel to the EoC occurs via a 21-bits data bus, therefore  
 451 only one clock cycle is needed and the dead time bottleneck is rather given by the  
 452 bandwidth of the serializer which trasmits data off-chip from the EoC. In our setup the  
 453 serializer operates at 40 MHz, thus to transmit a data packet (27-bit considering the ad-  
 454 dition of 6 bits to identify the double-column at the EoC) at least 675 ns are needed. For  
 455 what we have said so far, the R/O is completely sequential and therefore is expected a  
 456 linear dependence of the reading time on the number of pixels to read:

$$\tau = 25 \text{ ns} \times (\alpha N + \beta) \quad (2.15)$$

457 where  $\alpha$  and  $\beta$  are parameters dependent on the readout chain setting.

458 To test the linearity of the reading time with the number of pixels firing and to measure  
 459 it, I have used the injection circuit which allows me choosing a specific hit rate: I made  
 460 a scan injecting a fix number of pulses and each time changing the number of pixels  
 461 injected. Indeed the injection mode allows fixing not only the amplitude of the pulse,  
 462 which corresponds to the charge in DAC units, but also the time between two consecutive  
 463 pulses (DELAY). The hit rate then corresponds to 25 ns/DELAY.

464 Unfortunately a high random hit rate on the matrix cannot be simulated by the in-  
 465 jection because of the long time ( $\sim$ ms) needed to set the pixel registers of the injection;  
 466 then I was forced to specify at the start of the acquisition the pixels to inject on, and for  
 467 convenience I chose those on a same column. In figure 2.22 is shown the dependence of  
 468 the efficiency on the DELAY parameter in two different cases. For the 5 pixels example  
 469 the efficiency goes down the 90% at a DELAY of  $\sim$ 185 clock counts, which corresponds  
 470 to 4.625  $\mu$ s and to a rate of 216 kHz, while in the 10 pixels example, the efficiency goes  
 471 under the 100% at  $\sim$ 380 clock counts, which corresponds to 9.5  $\mu$ s and to a rate of 105 kHz.  
 472 From the efficiency curves I have then looked for the time when the efficency decreases.  
 473 In figure 2.23(a) is shown the dead time per pixels as a function of N with different R/O  
 474 parameters configuration, the meaning of which is explained in chapter ???. The default  
 475 value suggested by the designer of the chip are reported in table 2.4; moving too much  
 476 the readout parameters from the default ones, the readout does not work properly, and no  
 477 hits can be read at all. The problem probably stays in the firmware setting of the readout  
 478 which are specially fixed for our chip **Sul repository, nei commenti ci sono altri valori pos-  
 479 sibili per il FREEZE, ma avevamo detto che probabilmente sono relativi ai setting di altri  
 480 chip.** Despite the single pixel reading time does not depend on the position on the pixel  
 481 matrix, whithin a clock count which is  $\sim$ 25 ns, and it is equal to 106 clock counts, since  
 482 the  $\tau_d$  critically depends on the pixel position on the matrix: in particular the reading  
 483 sequence goes from row 224 to row 0, and from column 0 to column 112, making the pixel  
 484 on the bottom right corner the one with the longest dead time.

485 Furthermore to test that there is no dependece of the digital readout time from the

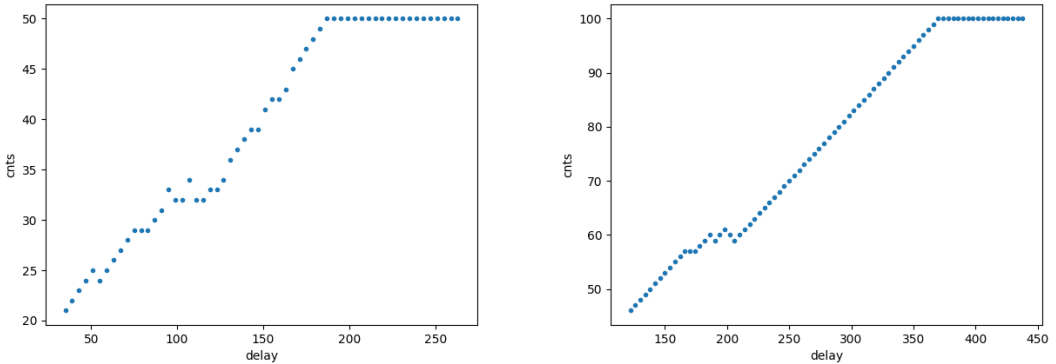


Figure 2.22: Efficiency vs the DELAY parameters. (a) I made a scan injecting 5 pixels with 50 pulses for each DELAY configuration and (b) 10 pixels with 100 pulses for each DELAY

Parameter	Value [DAC]	Value [ $\mu$ s]
START_FREEZE	64	1.6
STOP_FREEZE	100	2.5
START_READ	66	1.65
STOP_READ	68	1.7

Table 2.4: Default configuration of the R/O parameters

charge of the pulse, I have try to change the amplitude of the pulse injected, but the parameters found were consistent with the default configuration ones. No difference in the  $\alpha$  and  $\beta$  coefficients has been observed between the two case. Referring to eq.2.15, the factor  $\alpha$  is proportional to the difference (STOP\_FREEZE - START\_READ), while the offset  $\beta$  lies between 5 and 15 clock counts.

The readout time found by this test is so long because in the prototypes no parallelization of the informations (with the instruction of more serializer for example) and no storage memory are included; this feature are typically added in the final prototypes. An example closely linked to TJ-Monopix1 is OBELIX: it will include on the chip a storage buffer to optimize the dead time and to keep a low occupancy even at high fluence.

## 2.2 ARCADIA-MD1 characterization

Unfortunatly the characterization of MD1 has not yet been completed because of some problems with the functionality of the first chip we received on which we have been able to make only a few electrical and communication test in order to test the operations of the FPGA and the breakount board (BB). We asked for another chip then but we, due to delay in the extraction and the bonding of the wafer, have received it one week ago; an exhaustive characterization and testing of the new chip have been going on in the clean room on the INFN, and I am going to show here only some preliminary results.

The problem with the broken chip occurs when it is biased, in particular, when the HV voltage is lowered down 0V, the sensor requires too much power and a too high current draw sets. We have discussed the problem with the designers of the chip whose helped

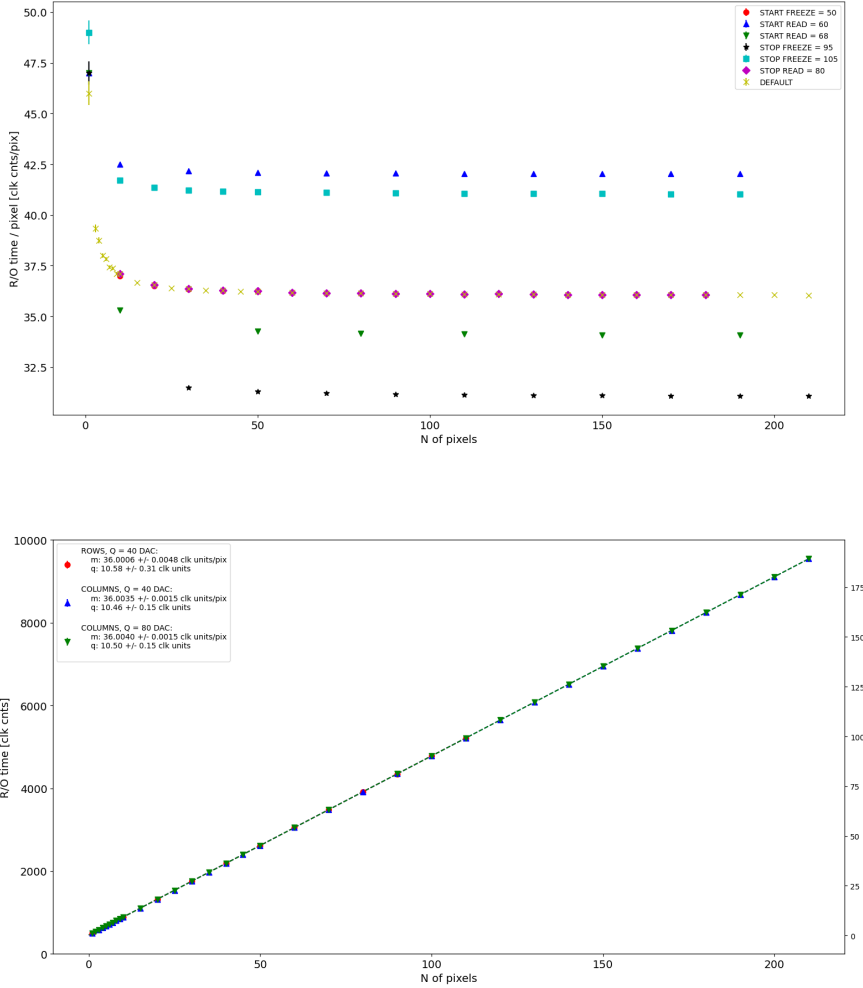


Figure 2.23: (a) Readout time per pixel as a function of the number of pixel injected obtained with different FE setup. (b) Readout time as a function of the number of pixels injected obtained injecting pulses with amplitude of 80 DAC (green), of 40 DAC on the same row (red) and on the same column (blue).

us indentifying the motivation of the break: the chip has been glued using too much conductive tape and hence have a short-circuit between the sides and the back, which makes impossible the biasing. Unfortunately, since both the sensor and the FE require at least -10 V to work properly, no measurement was possible except the acquisition of the noise in the FE circuit.

The second chip we received is a minid2, that is a "mini demonstrator" from the second submission. The two have the same charateristics but the minid2 is smaller than the MD1, in particular it only have  $32 \times 512$  pixels, instead of  $512 \times 512$ .

Up to now we used the injection circuit in order to make a threshold scan on a few pixels: differently from the TJ-Monopix1's charaterization where we performed a scan changing the injection charge of the pulse, with the minid2 we have instead changed the threshold (whose register is VCASN) keeping the charge of the pulse fixed. For each threshold we inject 100 pulses of amplitude  $10 \mu\text{s}$ . The dependence of the efficiency on the threshold for two pixels is shown in figure 2.25. Even if the behavior is reasonable, as the

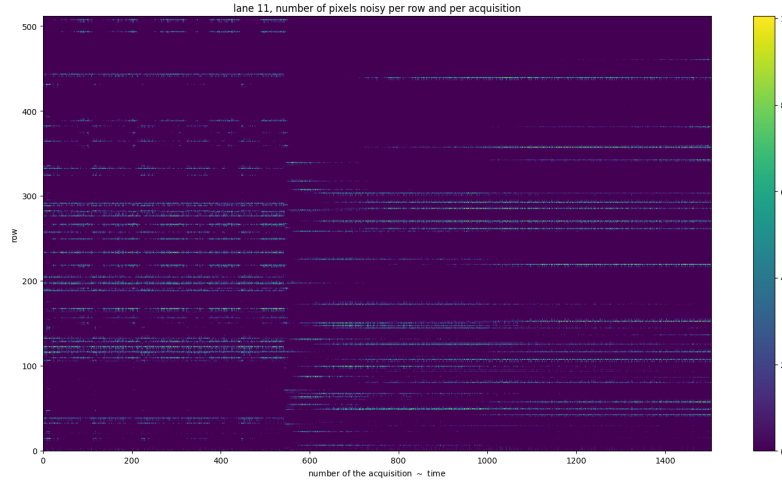


Figure 2.24: Noise in the front end circuit depending on the bias road across the matrix was recorded.

521 threshold is reduced the efficiency becomes higher, it is possible that the bias (-50 V) is not enough to full deplete the sensor, since the counts does not reach the 100% steadily.

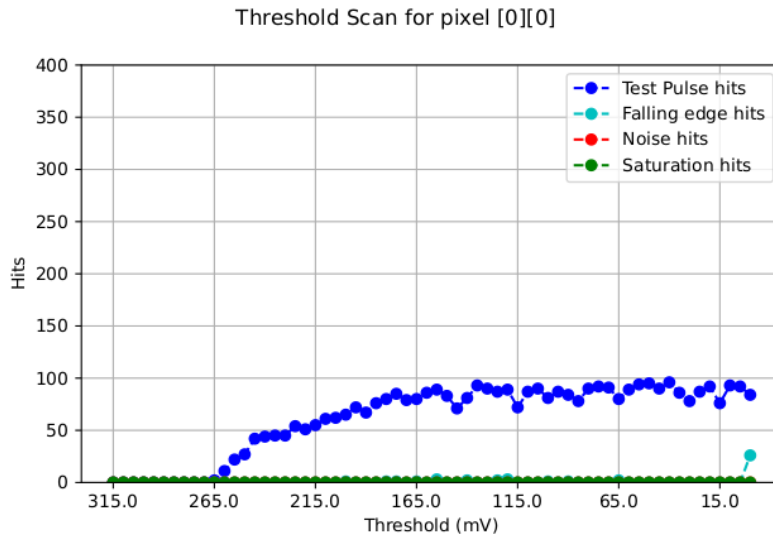


Figure 2.25: Threshold scan on the pixel (0,0). The sensors is polarized with  $\Delta V = -50$  V.

522  
523     The value of the SNR and the ENC Charge injection circuit uses  $C_{inj} = 2.325$  fF. The  
524     SNR, the ENC and the threshold dispersion on the matrix are expected to be respectively  
525      $\sim 90$ ,  $3 e^-$  and  $\sim 35 e^-$  with a detector capacity of 7 fF, that is about the capacity expected  
526     for the detector. The injection capacity is expected to be  $\sim 2.325$  fF, and in this condition  
527     the the minimum and maximum signals generated are respectively 0.08 fC and 2.6 fC.

528     Substantial differences have been observed with VCASN=40 DAC in both the efficiency  
529     and the threshold among the sections; this suggests that with this particular FE config-  
530     uration there is a big threshold dispersion on the matrix. The hitmap of an acquisition  
531     with the Fe55 source is shown in figure 2.26: the whole MD1 matrix with only the bottom  
532     region (32 rows) working is represented in (a), while in (b) there is a zoomed hitmap. The

533 rate seen within the region 8 (green region in the figure (a)) is compatible with the rate  
of the same radioactive source measured with TJ-Monopix1, that it  $\sim 3.3$  kHz. Looking to

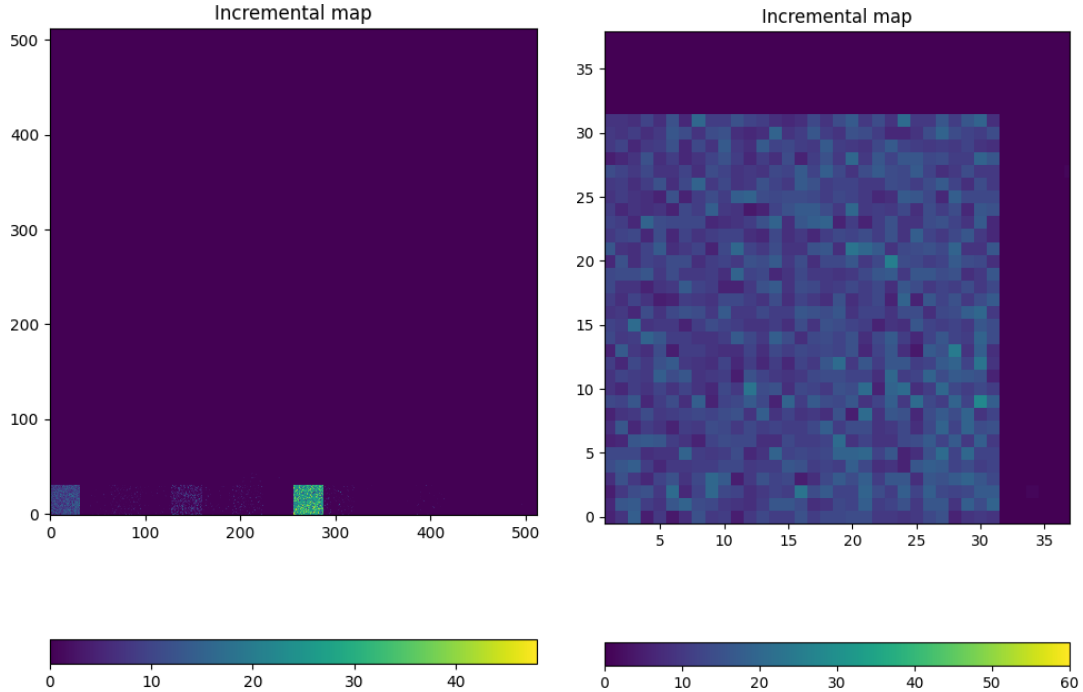


Figure 2.26: Fe55 acquisition with VCASN=40 DAC. (a) All the matrix  $512 \times 512$  is plotted even if the minid2 has only the rows in range 0-32. (b) A zoom on the first section (col 0-32).

534  
535 the Sr90 acquisitions (fig.2.27) many clusters and tracks can be immidiately distiguished,  
confirming what observed with TJ-Monopix1.

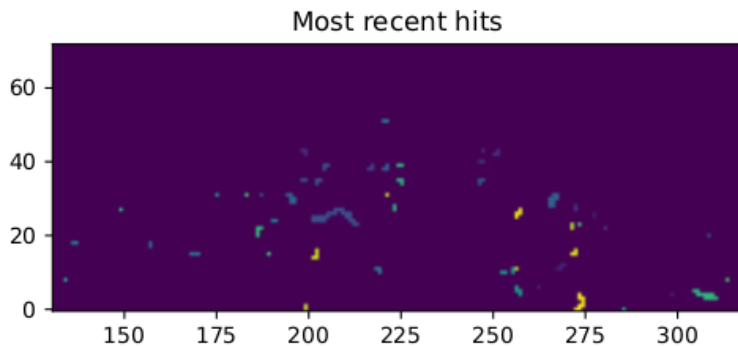


Figure 2.27: Sr90 acquisition with VCASN=40 DAC. The different colours are related with the time of arrival of the hits: in yellow the most recent hits, while in blue the old ones.

536

537 Chapter 3

538 Test beam measurements

539 During August 2022 a testbeam took place in Santa Chiara hospital in Pisa, where a  
540 new accelerator designed for both medical research and R&D on FLASH-RT, and for this  
541 reason called "ElectronFlash", have been installed a few months ago. The motivation  
542 of the testbeam measurements were testing TJ-Mopopix1 at high dose rate with a focus  
543 on investigating the possibility of the application in radiotherapy. Despite this particular  
544 device does not seem fitting the requirements imposed for that application, especially  
545 regarding the readout time, the measurements have been useful since help us characterizing  
546 the setup for future advance, and also give us the possibility of a complete characterization  
547 of the chip.

548 Given that in medical physics the dose is the standard parameter to characterize the  
549 beam, because of its obvious relation with the damage caused in the patient, I am going  
550 to explain the meaning of it by the point of view of the instrumentation. Infact, when  
551 interacting with measuring systems a more common and useful parameter is the rate or  
552 the fluence of particles. The conversion between the two quantity can be found thinking to  
553 the definition of dose: it is the concentration of energy deposited in tissue as a result of an  
554 exposure to ionizing radiation. Assuming total absorption of electrons in water, defined  
555 by law as the ordinary reference medium, the dose can be expressed as:

$$D[Gy] = \frac{NE[eV]}{\rho[g/cm^3]A[cm^2]x[cm]} \quad (3.1)$$

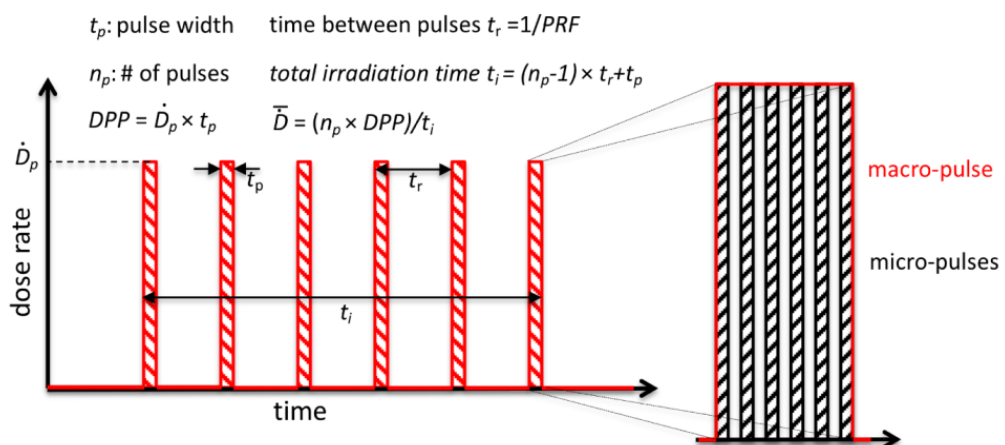


Figure 3.1: Typical beam structure of a beam used in electron radiotherapy

$\bar{D}$	Dose rate (mean dose rate for a multi-pulse delivery)	0.005-10000 Gy/s
$\dot{D}$	Intra pulse dose rate (dose rate in a single pulse)	0.01-1 $10^6$ Gy/s
DDP	Dose in a single pulse	0.04-40 Gy
PRF	Pulse repetition frequency	1-350 Hz
$t_p$	Pulse width	0.2-4 $\mu$ s
n	Number of pulses	single/pulse train

Table 3.1: The parameters that can actually be set by the control unit are the PRF, DDP,  $t_p$  and n (in particular the modality of singular irradiation or pulse train), while the other changes consequently.

556 After having applied the conversion of the energy from eV to J and noticed that  $E/\rho x$   
 557 roughly corresponds to the stopping power S of electrons in water, a simple estimation of  
 558 the dose released in water is:

$$D[Gy] = 1.602 \cdot 10^{-10} N[cm^{-2}] S[MeV cm^2/g] \quad (3.2)$$

### 559 3.1 Apparatus description

560 In order to shield the outdoor from ionizing radiation the accelerator is placed in a bunker  
 561 inside the hospital. The bunker has very thick walls of cementum and both the control  
 562 units of the accelerator and of the detector were placed outside in a neighbor room.

#### 563 3.1.1 Accelerator

564 The ElectronFlash accelerator is an electron Linear Accelerator (LINAC) with two energy  
 565 configurations, at 7 MeV and 9 MeV, and it can reach ultra high intensity (40 Gy/pulse)  
 566 keeping the possibility of accessing many different beam parameters and changing them  
 567 independently from each other, a characteristic that makes it almost unique worldwide  
 568 and which is fundamental for research in FLASH-RT, both for the medical aspects<sup>1</sup> and  
 569 for the studies on detectors. The accelerator implements the standard beam structure  
 570 used in RT with electrons (fig. 3.1), that is a macro pulse divided in many micropulses;  
 571 the parameters used to set the dose and their range of values settable by the control unit  
 572 is reported in table 3.1.

573 The accelerator is also provided of a set of triod cannons  $\sim 1.2$  m long and with diameters  
 574 in range from 1 cm to 12 cm and a collimator that can be used as beam shaper to  
 575 produce a squircle shape. The triode, which is made by plexiglass, must be fix to the gun  
 576 during the irradiation and is needed for producing, via the scattering of electrons with it,  
 577 an uniform dose profile (fig.3.2) which is desired for medical purpose.

#### 578 3.1.2 Mechanical carriers

579 The tested detector consists in one chip, the Device Under Test (DUT), mounted on  
 580 a board and connected to FPGA with same arrangement of figure 1.3. These boards  
 581 have been positioned vertically in front of the triode on a table specifically built for the

<sup>1</sup>For example, it is not yet really clear the dependence of the efficacy of the FLASH effect on the whole beam parameters

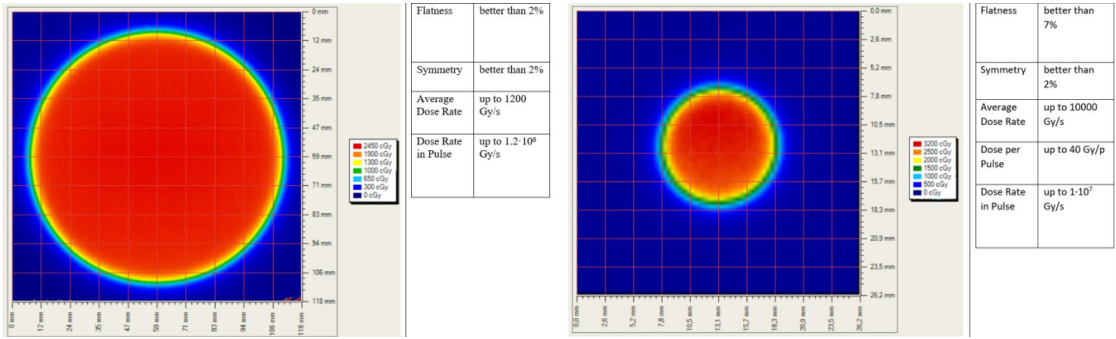


Figure 3.2: Two example of x-y isodose curves for two different triodes, 10 cm and 1 cm respectively, reported by the producer in the manual with the specific of the accelerator (S.I.T. - Sordina IORT Technologies S.p.A.). With the smaller collimator the dose rate in pulse is comparatively higher.

582 testbeam. The tree board have been enclosed in a box of alluminium with a window on  
 583 the DUT and with the required holes at the side to enable the biasing via cables and the  
 584 connection with the DAQ provided via ethernet cable. A trigger signal coming from the  
 585 control unity and syncronized with the pulses emitted from the beam has been also sent to  
 586 the FPGA. This digital signal cannot be considered a real trigger, since the TJ-Monopix1  
 587 prototype has been designed to be triggerless, but its Time of Arrival (ToA) had allowed  
 588 the reconstruction of the correct timing during the analysis.

589 In order to shield the sensor from the whole particles emitted from the gun, two  
 590 alluminium collimators have been fabricated: one has been positioned at the triode exit  
 591 while the other in front of the DUT. The collimators are  $t=32$  mm thick and have a  
 592 diameter  $d$  equal to 1 mm: assuming a beam divergence bigger than  $d/t=1/32 = 1.8^\circ$ ,  
 593 which is the case, the collimator at the triode output was supposed to work as a point  
 594 source and to reduce the rate on the DUT of a factor at least  $4 \cdot 10^{-4}$ . The second one,  
 595 being near the DUT, was instead supposed to shield the sensor from the electrons which  
 596 have passed the first one, except for a region of  $1 \text{ mm}^2$  configurable using *come si chiamano*  
 597 *quei cacciavitini per settare la posizione? sliding trimmer?*.

## 598 3.2 Measurements

599 Because of the dead time of TJ-Monopix1 it is not possible resolving the bunch sub-  
 600 structure and almost no one pixel can read more than a hit per bunch. I recall, indeed,  
 601 that the dead time per pixel depends on the location on the readout priority chain and  
 602 for each pixel  $\lesssim 1 \mu\text{s}$  are needed; therefore, assuming a pulse duration of  $4 \mu\text{s}$ , only a few  
 603 pixels at the top of the priority chain (placed at the upper left on the matrix) can fire a  
 604 second time, as they can be read a first time before the end of the pulse and then can be  
 605 hit again.

606 Since resolving the single electron track is impossible, a way this sensor could be used  
 607 in such context is reducing its efficiency and taking advantage of the analog pile up and  
 608 of the linearity of the analog output (ToT), in order to see a signal produced not by the  
 609 single particle but by more electrons. Reducing the efficiency and the sensibility of the  
 610 sensor is essential in order to decrease the high charge signal produced in the epitaxial  
 611 layer and mitigating the saturation limit: the smaller the output signal produced by a

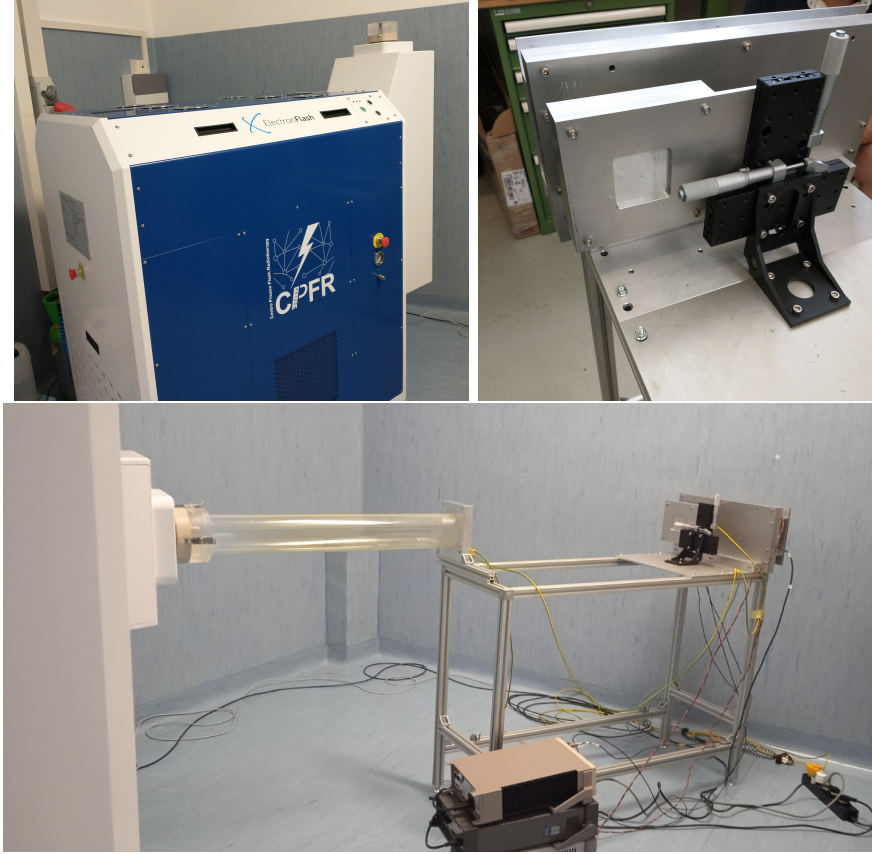


Figure 3.3: Experimental set up. (a) ElectronFlash accelerator: a rotating gantry allows the gun orientation from  $0^\circ$  to  $90^\circ$  (horizontal /vertical). (b) Collimator and DUT box. (c) Whole structure mounted: we used the 10 cm diameter and 1.2 m long triode; the DUT which is in the box behind the two collimators is connected to the power supply units.

particle and the higher the fluence the detector can cope with. There is an obvious limit in this context that is the ToT rollover, indeed, the signal stop giving information when this value has been overridden and is no more bijective. With the standard configuration of the FE parameters and the epitaxial layer completely depleted, a MIP produces a charge at the limit of representation with a 6-bit ToT; to obtain smaller output signals one can operate on the reduction of the gain.

Recalling the results in section 2.1.4, I have shown that concerning the PMOS flavor B, reducing the bias from -6 V to 0 V brings a reduction of efficiency down to 40 %, and a reduction in the gain of a factor  $\sim 1/3$ , while the reduction of the gain of the preamplifier allows a reduction of **circa 10, ma da controllare**.

In order to take advantage of the analog pile up and integrating the charge, for simplicity assume of two electrons, the second one must hit the pixel before the ToT goes under the threshold. The general condition is then  $\overline{\Delta T} < \overline{ToT}$ , but if a high  $P_\mu(n \geq 1)$  is required, a lower  $\overline{\Delta T}$  may be desired:

$$P(n \geq 1) = \sum_{n=1}^{\infty} \frac{e^{-\mu} \mu^n}{n!} = 1 - P(0) = 1 - e^{-\mu} \quad (3.3)$$

626

$$\mu = \frac{\overline{ToT}}{\overline{\Delta T}} \quad (3.4)$$

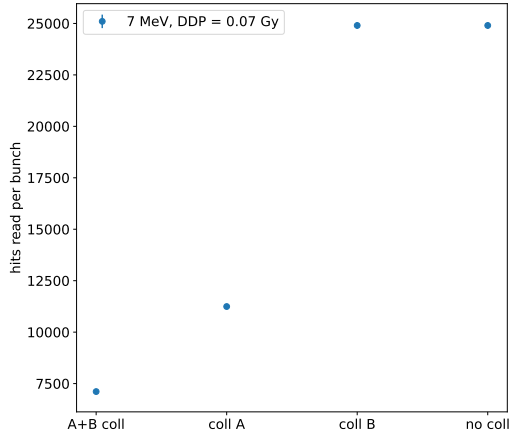


Figure 3.4: Mean number of hits read per bunch at DDP=0.07 Gy, with all the possible setup condition: with both the collimator, with only the collimator far from the chip (A), with only the collimator near the chip (B), and without any collimator.

627 If a  $P_\mu(n \geq 1) = 99\%$  then the  $\overline{\Delta T}$  must be  $\sim 0.22 \overline{ToT}$ . The ToT is in range [0,64] but  
 628 since the rollover must be avoided, the  $\overline{ToT}$  must be lower than 32, and then the minimum  
 629 rate on the pixel must be 1.25 MHz.

630  
 631 During the testbeam many runs have been performed, spanning the energy, the dose  
 632 per pulse and the four possible configurations with/without the collimators. We have  
 633 collected data with the PMOS flavor A in the standard configuration: with the PWELL  
 634 and PSUB biased at -6 V and set the standard default FE parameters reported in table  
 635 ???. During all the data acquisitions we have selected on the control unit of the accelerator  
 636 pulses with  $t_p$  of 4  $\mu$ m and with the smallest PRF settable, which is 1 Hz, in order to start  
 637 in the most conservative working point excluding the digital pile up of events from different  
 638 bunches. In these conditions, even if the whole matrix turns on, the total readout time  
 639 corresponds to  $25000 \times 1 \mu s = 25 \text{ ms}$  is still lower than the time between two consecutive  
 640 pulses. In figure 3.4 is shown the mean number of hits read during one accelerator pulse  
 641 in different setup conditions.

642 The readout starts with the trailing edge of the first pulse going down the threshold:  
 643 about 50 clk=1.25  $\mu$ s after this moment the FREEZE signal is sent to the whole matrix,  
 644 and the transmission of the data to the EoC begins. The hits read during the FREEZE  
 645 signal are the ones whose TE occurred before the start of the FREEZE and which have the  
 646 TOKEN signal high; the ones, instead, whose TE occur during the FREEZE are stored in  
 647 the pixel memory until the end of the FREEZE. At this point a second readout starts and  
 648 a second FREEZE is sent to the matrix. An example of the two sub-pulses corresponding  
 649 to an electron bunch is shown in figure 3.5: in the acquisition we injected 5 pulses with  
 650 both the collimators mounted on the table. Looking at the spectrum we can see that the  
 651 second sub-pulse has a populated tail on the right; this is due to the fact that the hits  
 652 which arrive before the start of the first FREEZE but have a long ToT that falls during  
 653 the FREEZE, are read at the second sub-pulse.

654 The 2D histograms in figure 3.5, reveal an important characteristics of our setup: in

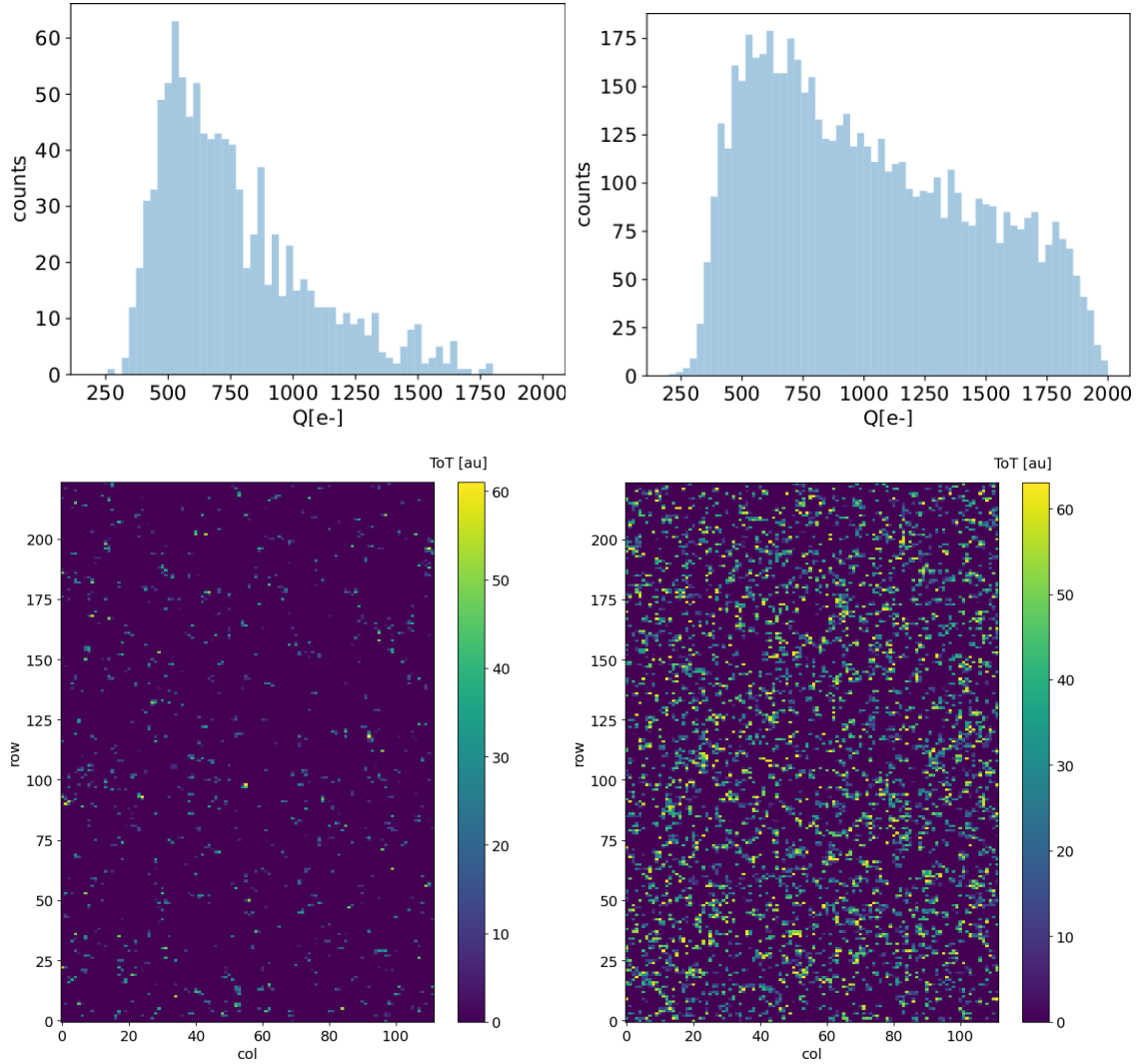


Figure 3.5: Acquisition with both the collimators: 5 pulses at  $DDP=0.07\text{ Gy}$ . (a) Spectrum of the charge released in the sensor: to apply the conversion I used the information found in the previous chapter. (b) 2D histogram of the ToT of the hits arrived in the sub-pulses.

fact, being uniform and not showing disomogenities, it follows that the collimators do not shield all the particles. We supposed that this was due to a Bremsstrahlung photon background higher than expected but a full verification of that and the analysis of the data is still going on. In figure 3.6, instead, the histograms with a higher DDP value is shown; in the example the matrix turns on completely, but again this happens in two different consecutive read chain.

When we have put aside the collimators, instead, the fluence increase a lot and the two-pulses substructure no more appears (fig. 3.7), but, because of the high attivity of the matrix, after each readout new hits with a fixed ToT were induced due to crosstalk. This problem had already been observed on other prototypes of TJ-Monopix1, and thanks to a simulation it has been observed that the main source of crosstalk is the voltage drop of the pre-amplifier ground as a result of the accumulated current that is drawn from the discriminator.

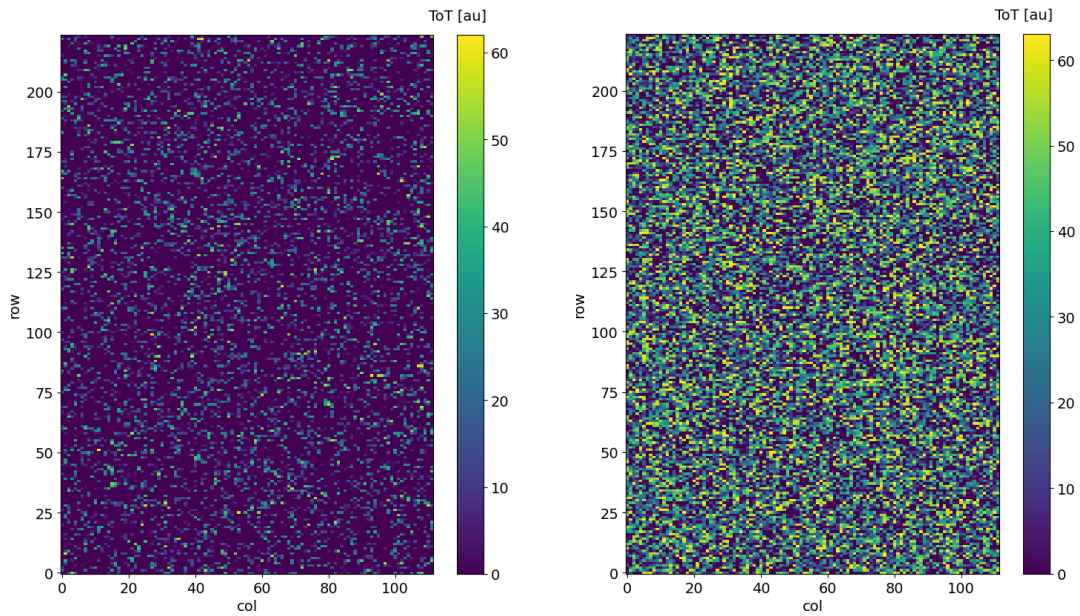


Figure 3.6: Acquisition with both the collimators: 5 pulses at  $DDP=0.6\text{ Gy}$ . 2D histogram of the ToT of the hits arrived in the sub-pulses. Compared with the previous maps, since the DDP is much higher, more pixels turn on.

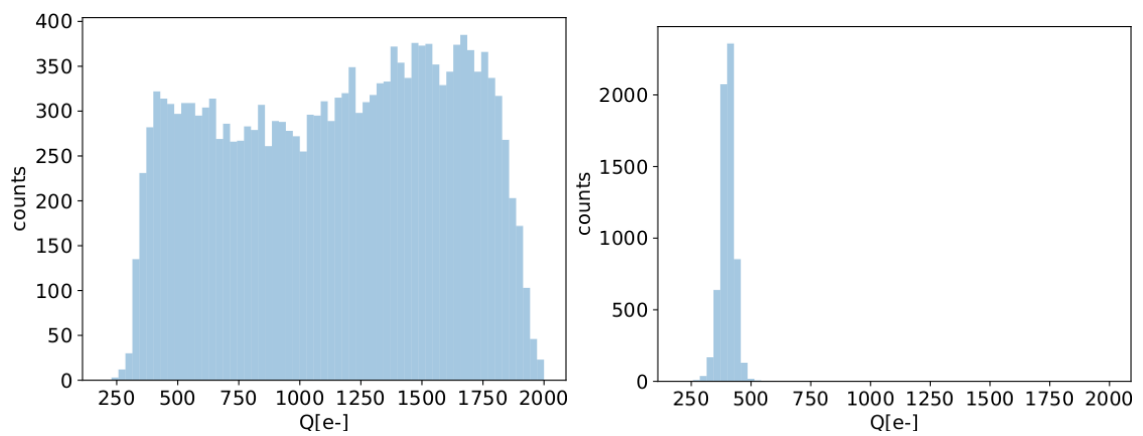


Figure 3.7: Acquisition without any collimator: 5 pulses at  $DDP=0.04\text{ Gy}$ .

# 668 Bibliography

- 669 [1] W. Snoeys et al. “A process modification for CMOS monolithic active pixel sensors  
670 for enhanced depletion, timing performance and radiation tolerance”. In: (2017).  
671 DOI: <https://doi.org/10.1016/j.nima.2017.07.046>.
- 672 [2] H. Kolanoski and N. Wermes. *Particle Detectors: Fundamentals and Applications*.  
673 OXFORD University Press, 2020. ISBN: 9780198520115.
- 674 [3] E. Mandelli. “Digital Column Readout Architecture for 10.1109/NSSMIC.2009.5402399  
675 the ATLAS Pixel 0.25 um Front End IC”. In: (2002).
- 676 [4] M. Garcia-Sciveres and N. Wermes. “A review of advances in pixel detectors for  
677 experiments with high rate and radiation”. In: (2018). DOI: <https://doi.org/10.1088/1361-6633/aab064>.
- 679 [5] C. Marinas. “The Belle-II DEPFET pixel detector: A step forward in vertexing in the  
680 superKEKB flavour factory”. In: (2011). DOI: [doi:10.1016/j.nima.2010.12.116](https://doi.org/10.1016/j.nima.2010.12.116).
- 681 [6] J. Baudot. “First Test Results Of MIMOSA-26, A Fast CMOS Sensor With Inte-  
682 grated Zero Suppression And Digitized Output”. In: (2010). DOI: [doi:10.1109/NSSMIC.2009.5402399](https://doi.org/10.1109/NSSMIC.2009.5402399).
- 684 [7] A. Dorokhov. “High resistivity CMOS pixel sensors and their application to the  
685 STAR PXL detector”. In: (2011). DOI: [doi:10.1016/j.nima.2010.12.112](https://doi.org/10.1016/j.nima.2010.12.112).
- 686 [8] Giacomo Contin. “The STAR MAPS-based PiXeL detector”. In: (2018). DOI: <https://doi.org/10.1016/j.nima.2018.03.003>.
- 688 [9] Nolan Espplen. “Physics and biology of ultrahigh dose-rate (FLASH) radiotherapy:  
689 a topical review”. In: (2020). DOI: <https://doi.org/10.1088/1361-6560/abaa28>.
- 690 [10] Fabio Di Martino et al. “FLASH Radiotherapy With Electrons: Issues Related to  
691 the Production, Monitoring, and Dosimetric Characterization of the Beam”. In:  
692 *Frontiers in Physics* 8 (2020). ISSN: 2296-424X. DOI: [10.3389/fphy.2020.570697](https://doi.org/10.3389/fphy.2020.570697).  
693 URL: <https://www.frontiersin.org/articles/10.3389/fphy.2020.570697>.
- 694 [11] M. Dyndal et al. “Mini-MALTA: Radiation hard pixel designs for small-electrode  
695 monolithic CMOS sensors for the High Luminosity LHC”. In: (2019). DOI: <https://doi.org/10.1088/1748-0221/15/02/p02005>.
- 697 [12] M. Barbero. “Radiation hard DMAPS pixel sensors in 150 nm CMOS technology  
698 for operation at LHC”. In: (2020). DOI: <https://doi.org/10.1088/1748-0221/15/05/p05013>.
- 700 [13] K. Moustakas et al. “CMOS Monolithic Pixel Sensors based on the Column-Drain  
701 Architecture for the HL-LHC Upgrade”. In: (2018). DOI: <https://doi.org/10.1016/j.nima.2018.09.100>.

- 703 [14] I. Caicedo et al. “The Monopix chips: depleted monolithic active pixel sensors with  
704 a column-drain read-out architecture for the ATLAS Inner Tracker upgrade”. In:  
705 (2019). DOI: <https://doi.org/10.1088/1748-0221/14/06/C06006>.
- 706 [15] D. Kim et al. “Front end optimization for the monolithic active pixel sensor of the  
707 ALICE Inner Tracking System upgrade”. In: *JINST* (2016). DOI: doi:10.1088/  
708 1748-0221/11/02/C02042.
- 709 [16] L. Pancheri et al. “A 110 nm CMOS process for fully-depleted pixel sensors”. In:  
710 (2019). DOI: <https://doi.org/10.1088/1748-0221/14/06/c06016>.
- 711 [17] L. Pancheri et al. “Fully Depleted MAPS in 110-nm CMOS Process With 100–300-  
712 um Active Substrate”. In: (2020). DOI: 10.1109/TED.2020.2985639.